Bachelor thesis 2026

Ride Height Control System for a Foiling Sailing Dinghy

Development of a Mechatronic control system
for the main foil of a SuMoth dinghy.

Edwin Ghasemi
Axel Gustafsson
Jack Kristensson
Tom Peleg
Samuel Rydz Wullens
Marcus Åkerskog

CHALMERS

Institution for Electrical Engineering
Chalmers Tekniska Högskola
Göteborg 2026

Ride Height Control System for a Foiling Sailing Dinghy
Development of a Mechatronic control system
for the main foil of SuMoth dinghy
E. Ghasemi, A. Gustafsson, J. Kristensson ,T. Peleg, S. Rydz Wullens, M. Åkerskog

Supervisor: Arturo Desaix Lopez Rojas, Department of Electrical Engineering
Examiner: Karinne Ramirez-Amaro, Department of Electrical Engineering

Bachelors thesis 2026
Department of Electrical Engineering
Chalmers university of Technology
SE-412 96 Göteborg
Telefon +46 31 772 1000

Abstract

This thesis aims to present the development of a mechatronic ride height control system for the Chalmers Formula Sailing moth dinghy Saga. Subsequently, the objective has been to create a system capable of riding at a set height above sea level in normal conditions.

Energy efficiency within the maritime industry has been a driving force for innovation in the field. Hydrofoiling is an old technology that has gained traction as it has been shown to be an effective alternative. However, as the maritime environment is unpredictable, challenges arise with the construction of a stable, reliable control system. With hydrofoiling not being a widely adopted technology, limited research has been made in mechatronic control systems for foiling watercraft. This thesis contributes to that research by sourcing components, designing and constructing parts, coding a regulator and finally building and testing the control system. The result showed data in which the regulator responded as expected based on the estimated height generated from the sensors. It was concluded that the physical system was sufficient, but further calibration of the controller was needed to reach the objective. It is believed that the project is a good platform for future work for the Chalmers Formula Sailing team.

Search terms: Hydrofoil, Mechatronic, Moth, SuMoth, Control system, Sailing, Foiling, PID

Preface

We would like to thank our examiner Karinne Ramirez-Amaro and supervisor Arturo Desaix Lopez Rojas for overseeing the project and for their invaluable input and guidance. Special thanks go to Chalmers Formula Sailing for lending us their Moth dinghy and countless hours of their time during field testing. We also extend our gratefulness to the staff at the FUSE and CASE makerspaces for providing their facilities and resources.

The Authors, Göteborg, May 2026

The Use of Artificial Intelligence (AI) Tools

To assist the project Large language models (LLM) were used, which includes ChatGPT and Claude. The tools were used for generating example codes as well as for explaining mathematical and engineering concepts. The output and information received from the tools have been initially reviewed by individually for relevance and accuracy. Further discussion internally within the group and with the supervisor was also conducted. Passing information was later challenged and revised using relevant academic journals and sources. The tools used were not applied to the creation of research content, data analysis or interpretation of the result. All scientific claims presented in this thesis are made by the authors.

Competing Interests

The authors acknowledge a potential conflict of interest in this project. Some of the material used, including photographs and technical information, was provided by Chalmers Formula Sailing. One of the authors has been actively involved in CFSail and was responsible for managing the project prior to the start of this thesis work. This prior involvement is disclosed as it may be relevant for the interpretation of the material presented. The matter has been discussed with the supervisor and the report has been prepared with the aim of maintaining objectivity and using independent sources where applicable.

Contents

List of Figures

List of Tables

Abbreviations

The following list presents the acronyms employed throughout this thesis together with their corresponding definitions.

ADC	Analog-digital converter
CFD	Computational fluid dynamics
CFSail	Chalmers Formula Sailing
EKF	Extended Kalman filter
FDM	Fused deposition modelling
FS	Fully submerged
I^2C	Inter-integrated circuit (communication protocol)
IDE	Integrated development environment
IMU	Inertial measurement unit
KF	Kalman filter
LLM	Large language model
LQR	Linear quadratic regulator
MCU	Microcontroller unit
PID	Proportional-integral-derivative
PLA	Polylactic acid (plastic polymer)
PETG	Polyethylene terephthalate glycol-modified
PWM	Pulse width modulation
SP	surface-piercing
SPI	Serial peripheral interface
UART	Universal asynchronous receiver/transmitter

List of Symbols

The following table contains descriptions and units for symbols used in the thesis:

Symbol	Description	Unit
α	Servo deflection angle	[rad]
F_{Lift}	Lift force produced by the foil	[N]
ρ	Fluid density	$[\text{kg}\,\text{m}^{-3}]$
S_{Foil}	Hydrofoil surface area	$[\text{m}^2]$
C_{L}	Coefficient of lift	dimensionless
$C_{\text{L}\theta}$	Angle dependant lift(foil)	$[\text{rad}^{-1}]$
$C_{\text{L}\delta}$	Angle dependant lift(flap)	$[\text{rad}^{-1}]$
v	Horisontal speed through water	$[\text{m}\,\text{s}^{-1}]$
m	Mass	[kg]
θ	Foil angle off attack	[rad]
δ	Flap deflection angle	[rad]
$\ddot{z}$	Vertical acceleration in vessel coordinate frame	$[\text{m}\,\text{s}^{-2}]$
$\ddot{z}_e$	Vertical acceleration in earth coordinate frame	$[\text{m}\,\text{s}^{-2}]$
z	Vessel ride height in earth coordinate frame	[m]
$\hat{z}_w$	estimated height at wand attachment point	[m]
$\hat{z}_c$	estimated height at the centre of the vessel	[m]

1

Introduction

The fastest way to move across water is to stop touching it. Achieving high performance in marine vessels, in terms of maximum attainable speed, hydrodynamic efficiency and stability, depends critically on minimizing the resistance between the vessels hull and the surrounding water [1]. The hull is the main structural body of a vessel, sitting in direct contact with the water surface and is the primary source of hydrodynamic drag. Until recently, marine vessels were primarily categorized as either displacement craft, where the hull is fully submerged and supported by the weight of water it displaces, or planing craft, where the hull skims across the surface using dynamic lift generated at speed [2], as can be seen in Figure 1.1. Both rely on sustained hull-water contact to remain afloat. This wetted surface area generates significant hydrodynamic drag, limiting both speed and efficiency. To reduce this drag, an alternative category was introduced, hydrofoiling, where submerged lifting surfaces generate lift instead of the hull itself, allowing the hull to rise clear of the water, reducing or eliminating hull drag altogether [3].

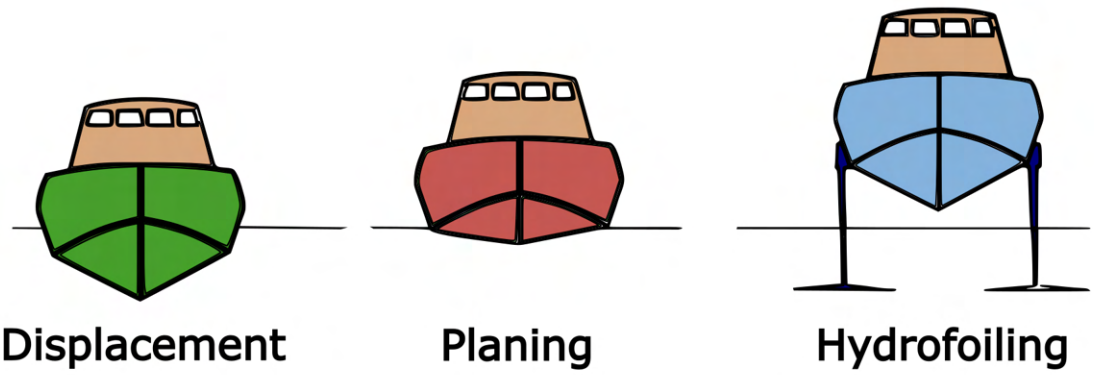

Figure 1.1. Frontal cross sectional view of displacement, planing, and hydrofoiling vessel modes. The coloured regions indicate the hull sections interacting with the water in each operating condition.

Hydrofoiling vessels employ one or more submerged lifting surfaces, known as hydro-

foils, mounted beneath the hull. As vessel speed increases, these foils generate lift, partially or fully raising the hull out of the water, a state commonly referred to as foiling or flying, seen in Figure 1.2. By reducing the wetted surface area, this enables higher operating speeds and improved energy efficiency compared to conventional displacement and planing vessels [4].

Figure 1.2. Illustration of a hydrofoiling vessel transitioning from hull-borne to foil-borne operation as speed and hydrofoil lift increase, reducing hydrodynamic drag.

While hydrofoiling significantly improves hydrodynamic efficiency, it introduces a fundamental trade-off between performance and stability. By lifting the hull clear of the water, the vessel loses the natural damping effect that hull-water contact provides as the water is no longer there to resist unwanted motion. Instead, the vessel's attitude and height become entirely dependent on the behaviour of the hydrofoils [5]. For fully submerged foil configurations, this creates an inherently unstable system. Small disturbances as a wave, a gust of wind or a subtle shift in speed can rapidly alter the lift generated by the foils causing the vessel to pitch, climb or dive if left uncorrected. Maintaining stable foil-borne flight therefore requires continuous active control, constantly adjusting the foils to regulate lift, pitch and ride height in real time. Designing a system capable of doing this reliably is one of the central challenges in high-performance hydrofoil development and the problem this project sets out to solve [6].

1.1 Hydrofoil

Hydrofoiling technology is not a recent innovation. The first documented hydrofoil vessels date back to the late nineteenth century and multiple successful hydrofoil projects were developed throughout the twentieth century [7]. Despite demonstrating performance advantages, widespread adoption remained limited for many decades, constrained by material, computational and control technology limitations [8]. In recent years, advances in composite materials, computational fluid dynamics and control technology have renewed interest in hydrofoiling. Increased public exposure through high-performance sailing competitions, such as the America's Cup [9] in the early 2010s and commercialization efforts by companies like Candela [10] have further accelerated this development. Today, hydrofoiling has expanded across the marine industry, from high performance racing classes such as the AC75, F50 and IMOCA60 fleets to commercial passenger ferries and military vessels [11]. Hy-

drofoils generate lift through the same fundamental principle as aircraft wings, a pressure difference created by fluid flow around the foil profile [12], illustrated in Figure 1.3. As vessel speed increases, the lift produced by the hydrofoils increases accordingly, and the specific profile shape determines the lift characteristics of the foil. When sufficient lift is generated, the hull is partially or fully raised out of the water, transitioning the vessel from a hull-borne to a foil-borne state [13], see Figure 1.2.

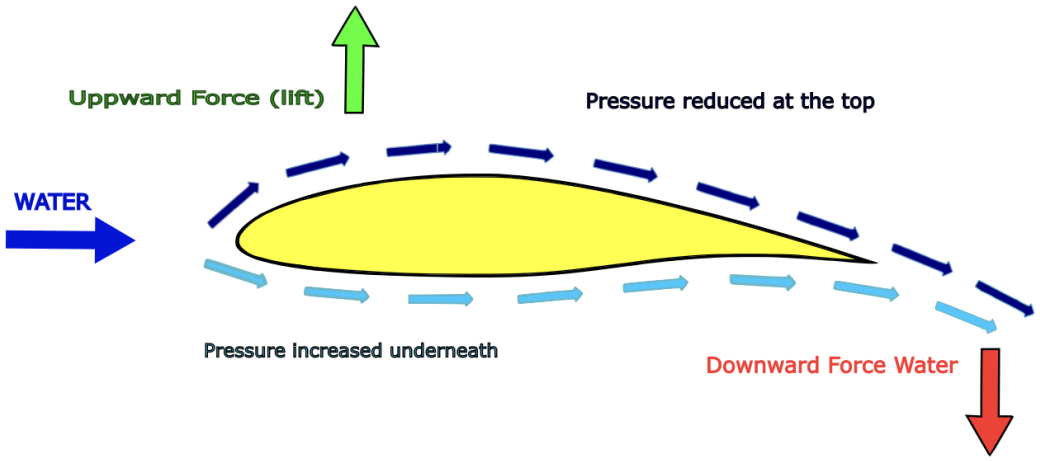

Figure 1.3. Pressure distribution around a hydrofoil profile; reduced pressure above and increased pressure below the foil generates a net upward lift force.

Hydrofoils exist in several shapes and configurations, including fully submerged (FS) foils such as T-foils, L-foils and C-foils, and surface-piercing (SP) configurations such as V- and U-foils [8], as illustrated in Figure 1.4. Each configuration is suited to different applications, offering different hydrodynamic and stability characteristics. Surface-piercing foils are generally passively stable, as changes in vessel velocity naturally regulate the generated lift, allowing them to operate without continuous active control [5].

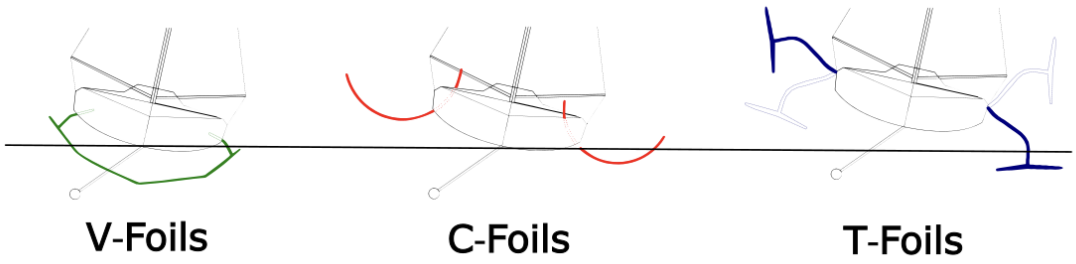

Figure 1.4. Frontal cross section of foil types and their respective placements in the water

However, this passive behaviour comes at the cost of higher hydrodynamic drag

and lower overall efficiency compared to FS configurations. L- and C-foils represent an intermediate solution, capable of operating both SP and FS, generating both vertical lift and lateral forces. Depending on their design and application, they can operate with limited active control, requiring only occasional adjustment of rake or immersion depth rather than continuous regulation [14]. Fully submerged foils, such as T-foils, offer the highest hydrodynamic efficiency but are not inherently self-stabilising, requiring continuous active control to regulate lift and maintain the vessel fully foil-borne. This makes them the most complex to implement, but also the preferred choice in high-performance applications and the focus of the remainder of this report [15].

1.1.1 International Moth Class and SuMoth

This project focuses on a foiling dinghy competing within the International Moth class, showcased in Figure 1.5. Sailing classes vary in how strictly they regulate boat design. One-design classes mandate that all boats are built to an identical blueprint using the same materials and components to ensure equal performance between competitors. Development classes instead usually only define a set of dimensional constraints, known as a box rule. This allows designers freedom to innovate within those limits [16].

Figure 1.5. Chalmers Formula Sailing's Moth Saga foilborne on lake Garda

The International Moth is one such development class, governed by a box rule with a maximum hull length of 3.355 metres, a maximum beam of 2.250 metres and a sail area capped at 8.25 square metres, but no restrictions on materials, hull weight or construction methods, illustrated in figure 1.6. The International Moth is therefore defined as a single-handed, open development class dinghy, governed by

these dimensional constraints. This means that no two boats on the starting line need to be identical[17].

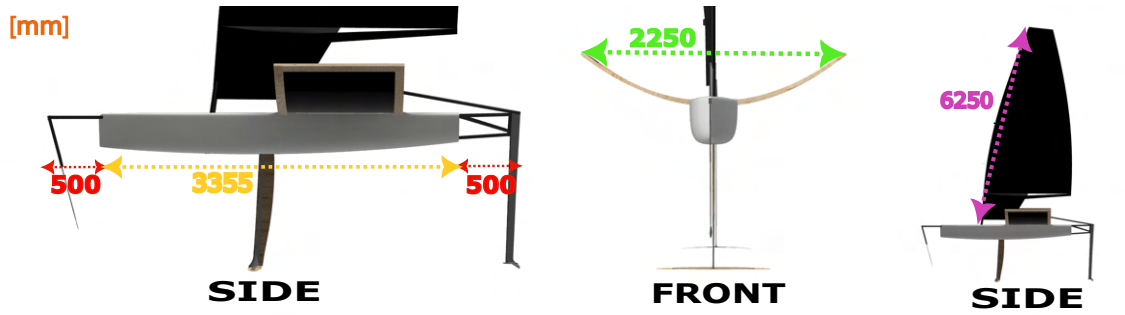

Figure 1.6. International Moth box rule measurement

The design freedom of the box rule has driven technological development within the class. Foiling is the most significant example, experimentation with hydrofoils in the early 2000s demonstrated clear performance advantages over traditional displacement designs, leading the class to evolve in that direction. Each new iteration of the boat has since introduced further developments, advancing the class as a whole [18]. Today, the modern International Moth is a fully foiling single-handed dinghy employing a T-foil configuration, with a main lifting foil mounted on the main vertical foil and a smaller control foil on the rudder vertical foil, as illustrated in Figure 1.7. The class t conditions between 6 and 25 knots, and once foiling, bo above are common, with peak speeds exceeding 40 knots

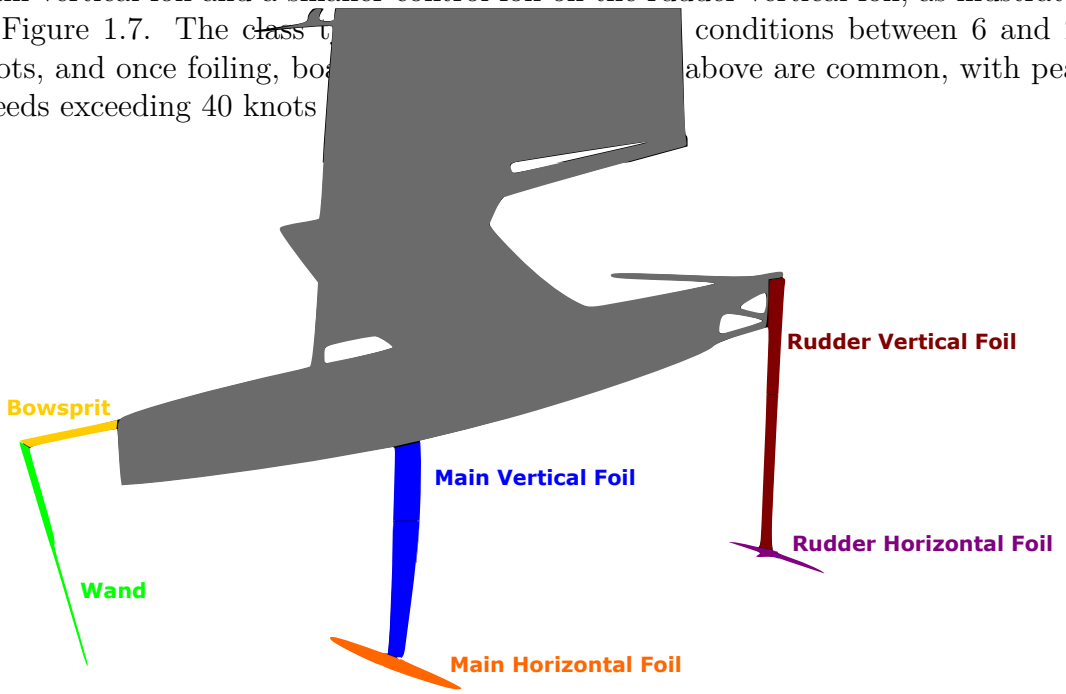

Figure 1.7. Side view of a foiling International Moth, illustrating the key components including the bowsprit, wand, main vertical foil, main horizontal foil, rudder vertical foil and rudder horizontal foil.

The boat used in this project, *Saga*, as can be seen in Figure 1.5, is designed and manufactured by the student team Chalmers Formula Sailing, CFSail, at Chalmers University of Technology. *Saga* was constructed to participate in the SuMoth class, competing in what is called the Sustainable Moth Challenge. Hereafter, the boat will be referred to as *Saga*. The SuMoth class is based on the International Moth class but differs in two significant ways: it introduces additional rules regarding the environmental impact of the boat and it permits the use of electronic control systems. The latter represents a fundamental departure from the International Moth class, where no active electronic systems are permitted, except for data collection purposes [19].

1.2 Control System of the Moth

The ride height of the boat is controlled by a mechanical system using a wand attached to the front of the boat, as seen in Figure 1.9. When the hull is close to the water, the wand tip deflects, causing the wand to rotate around its pivot point on the bowsprit. Through a series of linkages, this rotation changes the angle of attack of the trailing edge of the main foil, the flap, see Figure 1.10. The closer the boat is to the water, the greater the angle becomes, increasing lift and pushing the boat upward. As it reaches the desired flight height, the wand follows the water surface and decreases the attack angle of the foil allowing it to return to a neutral position, keeping the boat approximately parallel to the water [20]. This behaviour is illustrated in Figure 1.8.

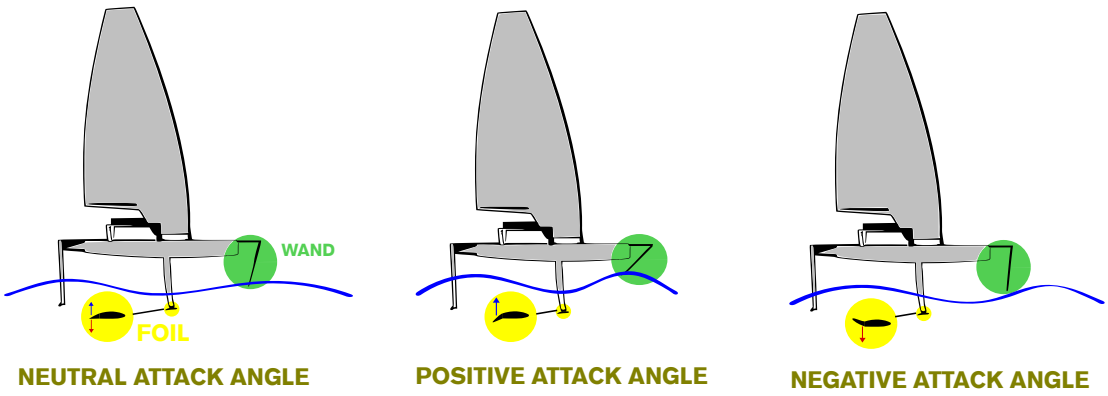

Figure 1.8. Correlation between wand angle and foil angle of attack; neutral (left), positive angle of attack generating lift (centre), and negative angle of attack reducing lift (right).

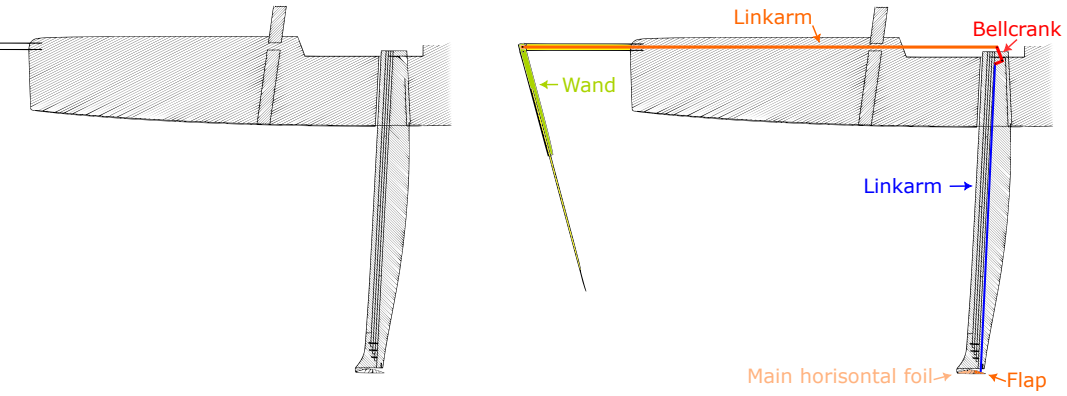

Figure 1.9. Overview of the mechanical wand-based control system for a Moth, showing the wand, linkarms, bellcrank and main horizontal foil with flap.

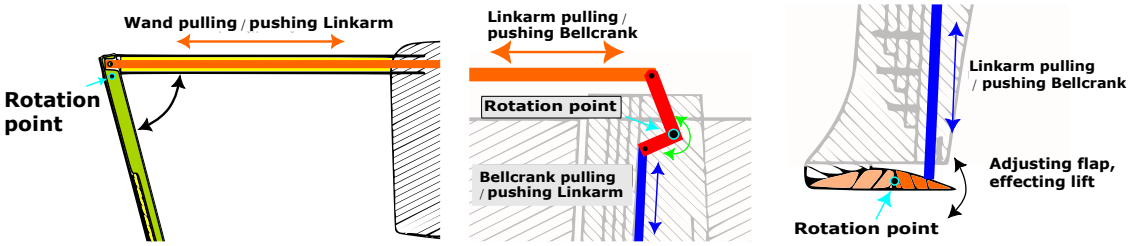

Figure 1.10. Mechanical linkage sequence of the wand control system; wand rotation pulling the linkarm (left), bellcrank translating horizontal motion to vertical (centre), and linkarm adjusting the flap angle of the main foil (right).

Foiling vessels are prone to "porpoising", a self-reinforcing cycle where the vessel repeatedly pitches nose-up and nose-down, unable to settle at a constant flight height [21]. Because the mechanical system responds only to changes in local wave height, this instability becomes increasingly difficult to control in irregular wave conditions or when encountering unexpected disturbances, potentially resulting in significantly increased drag or in severe cases, the boat being launched out of the water, as illustrated in Figure 1.11. A stable flight is therefore defined as one where the boat maintains minimal vertical movement while keeping the hydrofoils fully submerged as it's foiling.

Figure 1.11. Illustration of foil-induced launch. The control system reacts to an incoming irregular wave by increasing foil lift, but as the wave passes and the water surface returns to normal, the excess lift launches the vessel clear of the water.

In aircraft, the challenge of maintaining stable flight has long been addressed through active electronic control systems [22]. Much like a hydrofoiling vessel encountering waves and gusts, an aircraft must continuously compensate for atmospheric disturbances and therefore much of the same principles can be applied to hydrofoiling vessels [23].

An electronic control system could solve this issue while offering several additional advantages beyond basic stability. By actively monitoring the boat's height above the water surface using electronic sensors, the system can adjust the foils attack angle in real time with a greater precision than a purely mechanical solution. This enables more accurate height regulation, reduces vertical oscillation, and lessens hydrodynamic drag from excessive foil adjustments while maintaining stable flight. Furthermore, electronic control allows for software based tuning and implementation of advanced control strategies such as adaptive or predictive algorithms. Integrated data collection also makes performance analysis and system optimization more accessible [24].

1.3 Related Work

Similar research and projects have been made for hydrofoiling control systems. The scope and capabilities varies between different models of sailboats and motorboats. The variation results in different solutions and issues.

Among more advanced applications, one Americas cup AC45 class 45-foot long catamaran vessel uses a full state feedback (FSF) control system [25]. By modelling the behaviour of the boat with six DOF, accurate movement tracking is made during manoeuvrers. The boats are equipped with an Internal navigation system (INS) acting as an observer and processing data from an IMU as well as a GPS. The data is then fused with the data from an ultra sound sensor. Systems with solely measurements of the height above the water are burden by issues in determining the

systems state. A six DOF model and sensor fusion presented allows for smoother foiling dynamics handling the issue of a varying environment created by the waves.

Bai and Kim [26] compare the motion response between PID, LQR and Sliding mode control algorithms for regular and irregular wave conditions in simulations. They mention that LQ optimal control theory has been the favourable by theoretical researches whilst PID is the most used for motion control systems. Sliding mode control however is a less tested method. Results shows that the Sliding motion control performs poorly whilst the disturbance data is limited. The PID performs well in regular waves but due to disturbances created by the irregular waves it becomes unstable. The LQR performed well in both conditions which seems as to be a very promising option. However, the implementation of an LQR would come with its own difficulties. In a separate report simulations made by Chatzakis [27] concluded the systems potential but that a state-space model such as LQR is highly dependent on "available information on the vessel dynamics". The argument is further strengthened by Kim and Yamato [28], which conducted an experimental study testing the performance of a LQR control system on a vessel in waves. It concluded that a LQR needs extensive dynamic modelling, specifically wave disturbance and foil lift variation to perform well.

1.4 Problem Description

The mechanical control system used on *Saga*, the CFSail's Moth, has several identified limitations. One limitation arises from the mechanical linkage system directly connecting the wand and the flap, see Figure 1.9. This means that any adjustment to the wand directly affects the flap angle. As the wand responds to variations in the water surface, it influences flap position accordingly. This may result in a system with high sensitivity to small surface irregularities.

Irregular wave conditions can lead to instability in the system, where unusually large waves may cause excessive foil lift and loss of water contact, potentially resulting in a crash. Similarly, regular periodic waves introduce a limitation through wave-induced wand motion, which directly affects flap position and ride height and can amplify the porpoising behaviour described in Section 1.2.

The flexibility of the control system is also limited, as adjustments such as ride height reference, system sensitivity, and wave responsivity are constrained. While wand length can be adjusted by the sailor to modify ride height on the water, system sensitivity can only be adjusted on land by changing the bellcrank gearing. However, the system responsiveness is inherent to the mechanical design and cannot be adjusted, as the system will always respond to wave input.

The aforementioned limitations and problems with the mechanical regulator highlight the need for a more robust and flexible control approach, motivating the foundation of this thesis.

1.5 Objective

The general objective of this thesis is to design and implement a mechatronic ride height control and data acquisition system for the Chalmers Formula Sailing Moth dinghy, *Saga*. The system is intended to operate under typical sailing conditions, defined as wind speeds between 6 and 25 knots and wave heights up to 0.4 m.

This can be further broken down into particular objectives, which are:

- Develop a platform capable of measuring and collecting data on the ride height, as well as other relevant boat dynamics.
- Implement a mechatronic system that can control the flap angle based on the measured ride height.
- Design, implement a control system that maintains a set ride height.
- Tune and validate the mechatronic control system so that its performance matches or surpasses the mechanical one.

1.6 Scope and Constraints

To be able to complete the objective of the thesis within in the time frame the following items cover the scope:

- The focus of this project is to design and implement a mechatronic control system specifically for *Saga*. Consequently, the system is not designed with ease of mass production as a primary requirement.
- During the SuMoth Challenge, Saga competes against other student built SuMoth-class boats in multiple short races, approximately 10–20 minutes, over the course of a week. Racing is only conducted when conditions are within the operational limits of the boats and are considered safe, with no races held in wind speeds above 12 m/s or in conditions deemed unsafe for sailors or equipment. Consequently, the analysis in this thesis is restricted to these operating conditions.
- In-depth computational fluid dynamics (CFD) analysis is outside the scope of this project due to limitations in time.
- The mechatronic control system will be based on the existing mechanical design, retaining a wand connected to the bowsprit as the primary input for adjusting the bellcrank and, consequently, the flap angle, with no mechanical connection between the two

Within the scope of the thesis, the following obstacles and limitations constrained the project:

- The available budget consists of the budget provided by Chalmers as well as the contributions from CFSail1.7. As a result, any solutions outside this time frame and budget is considered outside the scope of this project.
- There will be limited opportunity to evaluate and adjust the mechatronic system. This is due to the short period over which the project will be carried out and only a small fraction of the project time has suitable weather for system validation.

1.7 Budget

The project operated under two separate budgets: a budget provided by Chalmers and an external budget funded by CFSail. The school budget was set at 5 000 SEK, of which 4 219 SEK was utilized, leaving a surplus of 781 SEK. Procurement through the school budget covered key electronic components including ESP32 microcontrollers, BNO085 IMU sensors, an IP69K-rated absolute encoder, waterproof M12 connectors and LiPo batteries. The external budget, contributed by CFSail, amounted to 2 215 SEK and covered servo actuators, enclosures, composite materials, and consumables. In total, the project expenditure across both budgets amounted to 6 315 SEK.

2

Theory

This chapter describes the theoretical foundations of the project. It presents equations describing foil behaviour that are central to the thesis. Mechatronics theory, such as uncertainty and filtering of signals, as well as regulator types, is also presented in this chapter.

2.1 Hydrofoils and Forces

To rise above the surface, the lift force of the foil must be larger than the gravitational forces acting on the boat and sailor. Once the boat rises above the surface to the desired ride height, these forces should be at equilibrium, keeping the boat at a constant height. The principle for maintaining a correct ride height can be derived from Newtons first and second laws, as presented in equation 2.1:

$$F_{\text{Lift}} = m \cdot g \tag{2.1}$$

The lift produced by the foil is dependent on the velocity v, area S, lift coefficient C_L, and density of the surrounding fluid ρ [29], as follows:

$$F_{\text{Lift}} = \frac{1}{2}\rho v^2 S_{\text{Foil}} C_L \tag{2.2}$$

Further, C_L describes how much lift is generated depending on the shape of the foil. In order to obtain a linear estimate of C_L, it can be broken down into multiple parts, as follows:

$$C_L = C_{L0} + C_{L\theta}\theta + C_{L\delta}\delta \tag{2.3}$$

Here, C_{L0} is the lift generated by the inherent shape of the foil. $C_{L\theta}$ describes how the lift depends on the angle of attack of the foil θ. Similarly, $C_{L\delta}$ describes the

extra lift generated by different angles of the flap, δ. The previous equations can be combined to obtain the full lift equation, as follows:

$$mg = \frac{1}{2}\rho v^2 S_{Foil}(C_{L0} + C_{L\theta}\theta + C_{L\delta}\delta) \tag{2.4}$$

2.2 Linearised Model

A way to simplify analytics without losing much of the realistic behaviour, is to linearise the system around an operating point [30]. An operating point is a configuration of parameter values that result in force equilibrium. The total lift force is then treated as some base lift, L_0, and small deviations around that point, ΔL. The deviations are estimated using first order taylor expansion, as follows:

$$\Delta L = \frac{\partial L}{\partial v}\tilde{v} + \frac{\partial L}{\partial \delta}\tilde{\delta} + \frac{\partial L}{\partial \theta}\tilde{\theta} \tag{2.5}$$

Where $\tilde{v}$, $\tilde{\delta}$, and $\tilde{\theta}$ represent small deviations from an operating point. Furthermore, let v, δ, and θ denote the actual values, and let v_0, δ_0, and θ_0 denote the corresponding operating-point values. Their relationship can then be expressed as follows:

$$v = v_0 + \tilde{v}, \quad \theta = \theta_0 + \tilde{\theta}, \quad \delta = \delta_0 + \tilde{\delta} \tag{2.6}$$

Using Newton's second law, small deviations around the operating point can be related to deviations in vertical acceleration, $\ddot{\tilde{z}}$, according to

$$m\ddot{\tilde{z}} = \Delta L \tag{2.7}$$

This relation makes it possible to determine the vertical acceleration, $\ddot{\tilde{z}}$, from the input variables v, θ, and δ.

2.3 Control System and Signal Processing

The following section provides a theoretical overview of relevant control theory and its role in the development of a functional mechatronic system.

2.3.1 PID Regulator

A PID controller is one of the most commonly used control strategies. It does not require an accurate system model, making implementation simple. The controller consists of three components: a proportional term, an integral term, and a derivative term [31]. The standard form of the PID controller is as follows:

$$u = K_p e(t) + K_i \int e(t)\,dt + K_d \frac{d}{dt} e(t) \tag{2.8}$$

Here, $e(t)$ is the error, defined as the difference between the desired value and the measured value. K_p, K_i, and K_d are gains for the proportional, integrating, and derivative parts.

2.3.2 Anti-Windup Theory

Every physical actuator possesses inherent mechanical limits, a state known as saturation. When a control signal reaches these limits, the feedback loop is effectively broken as the actuator can no longer respond to further increases in the control command.

If a PID regulator continues to integrate the error during saturation, the integral term will grow to an excessively large values, a phenomenon known as *Integrator windup*. This accumulated error forces the actuator to remain at its limit even after the error changes sign, until the integral term has sufficiently discharged. This leads to significant time delays and large overshoots. To mitigate this, *anti-windup logic* is applied to pause or limit the integration process whenever saturation is detected. [32]

2.3.3 Digital Filtering

Digital sensors often capture high frequency noise that does not represent the physical state of the system. To isolate the desired signals, recursive filters like exponential moving average (EMA) are used. The EMA provides a weighted average where newer samples have more influence.

$$y[k] = \alpha \cdot x[k] + (1 - \alpha) \cdot y[k-1] \tag{2.9}$$

where:

- $y[k]$ is the current filtered output.
- $x[k]$ is the current raw sensor input.
- $y[k-1]$ is the filtered output from the previous time step.
- α is the smoothing factor ($0 < \alpha \leq 1$).

The parameter α determines the filter's cutoff frequency and its dynamical response. A smaller α provides superior noise rejection but introduces significant phase lag. In practice this adds time delay into the signal, which can destabilize the control loop. In contrast, a α closer to 1 provides a faster response but allows more high frequency noise to pass through the regulator. [33]

2.3.4 Kalman Filter and Extended Kalman Filter

The Kalman filter (KF) is a recursive state estimation algorithm that provides optimal estimates of the internal state of a linear dynamic system from a sequence of noisy measurements. In context, a state vector represents the systems internal state, such as position, velocity as a set in a vector. The filter addresses the problem of estimating a hidden state vector, x_k, by fusing a dynamic model with measurement data while accounting for process noise (w_k) and measurement noise (v_k).

It allows for the estimation of variables that are not directly measurable, by combining multiple sensor inputs into a single state vector. Furthermore, it provides a statistical framework to account for non-modelled dynamics, such as wave and speed disturbances.

While the standard KF is optimal for linear systems, boat dynamics particularly involving rotations and hydrodynamic forces are inherently nonlinear. To address this, the Extended Kalman Filter (EKF) is employed. The EKF linearizes the nonlinear transformations about the current mean and covariance using Taylor series expansions (Jacobians). This allows the filter to estimate states in more complex scenarios where the relationship between the state and the measurements, or the state transition itself, does not follow a simple linear path.[34].

While these state-space models offer high precision, their performance is highly dependent on having accurate information regarding the system boat dynamics and the appropriate tuning of noise covariance matrices [35].

2.4 Sampling and Quantization

Sampling is the process of reducing a continuous time signal to a discrete time signal. Sampling refers to measuring the value of a continuous time signal at a predetermined frequency. The frequency is referred to as the sampling frequency and determines the speed at which a signal is processed. The inverted frequency reveals the time between each measurement in seconds [36].

The process of quantization describes the scaling of a discrete time signal. The amplitude of each measured sampling value is approximated to a finite set of discrete values. This process generates a sequence of quantization errors that describes the stochastic properties while approximating the sampled value. The sequence of errors creates a signal that is referred to as quantization noise. It is depicted as a disturbance whilst processing the signal. [36]

When choosing the frequency of which data is sampled, also known as sample rate, the Nyquist-Shannon theorem should be considered. This states that when discretely sampling a signal with a maximum frequency component $f_{\max}$, the sample frequency should be chosen according to:

$$f_{\mathrm{s}} \geq 2f_{\max} \tag{2.10}$$

Any frequency higher than $f_{\max}$ not handled by some kind of anti-aliasing filter will be mirrored in the Nyquist frequency and show as a low frequency alias in the frequency domain [37]. It is worth noting that, despite the Nyquist-Shannon theorem describing the lowest frequency needed to be able to fully reconstruct a signal with a frequency of $f_{\max}$, it is usually not considered enough to control a system with a closed loop bandwidth of f_{bw}. A more common rule of thumb is that for control, $f_{\text{s}} > 20 f_{\text{bw}}$.

2.5 The Hall Effect

The Hall Effect measures the orientation of a magnetic field. The Hall Effect is a physical phenomenon that occurs when a magnetic field is applied to a conductor, exerting a Lorentz force on the electrons inside the sensor. This force causes charge separation, pushing electrons to one side of the conductor and creating a measurable potential difference known as the Hall voltage. [38]

2.6 Pulse Width Modulation

Pulse width modulation (PWM) is a technique used to encode a message or control signal into a pulsing electrical voltage. In the context of digital rotary actuators, PWM is the standard communication protocol used to dictate the desired angular position of the output shaft. [39]

The signal consists of a periodic square wave, where the fundamental parameter is the pulse width. The duration the signal remains in a high state (t_{on}), typically measured in microseconds or as a duty cycle (D) derived as seen in equation (2.11). The following figure describes the form of such square wave 2.1.

$$\text{Duty cycle } D = \frac{t_{on}}{T} = 50\% \tag{2.11}$$

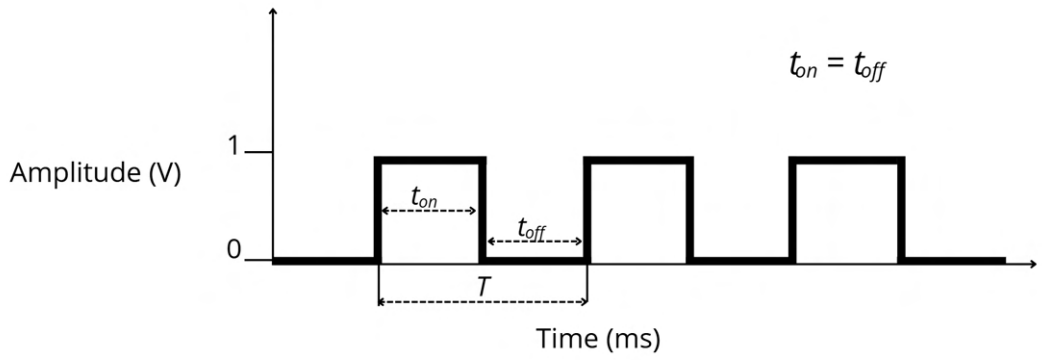

Figure 2.1. Example of a PWM square wave with 50% duty cycle

2.7 Inertial Measurement Unit

An inertial measurement unit (IMU) is an electronic device that measures and reports a body's acceleration, angular rate and the magnetic field surrounding the body. In the context of an active mechatronic control system on a foiling sailboat, an IMU can have a key role. It can provide continuous data about boat orientation and dynamic movements, essential to the state estimation algorithms, such as the Kalman filter described in Section 2.3.4. The IMU utilizes accelerometers and gyroscopes.

The accelerometer measures the specific force acting on the device along its sensitive axis. It captures both dynamic acceleration, caused by physical movement and static acceleration. By measuring the direction of the gravitational vector when the boat is relatively still, the accelerometer provides an absolute reference for the boats roll and pitch angles.

The gyroscope measures the angular velocity around the three axes of the system. The gyroscope is largely unaffected by linear forces or bumps from waves, making it fast and accurate at capturing rotational dynamics.

The IMU module outputs orientation in the form of a quaternion rotation vector, $q = (w_q, x_q, y_q, z_q)$, and acceleration as a linear acceleration vector, $f = (\ddot{x}, \ddot{y}, \ddot{z})$, expressed in the sensor's local coordinate frame. Since the ride height, z_e, is defined in the Earth fixed coordinate frame, the acceleration measurements must be transformed to the same coordinate frame in order to obtain correct information about ride height stability. This transformation is visualized in Figure **??**. The acceleration vector in the Earth fixed frame, $f_e = (\ddot{x}_e, \ddot{y}_e, \ddot{z}_e)$, can then be obtained as follows [40]:

$$f_e = q \cdot f \cdot q^{-1} \tag{2.12}$$

Since this transformation is linear, an equivalent transformation matrix, $C_e(q)$, can be defined such that the relationship between the coordinate frames can be expressed as follows:

$$f_e = C_e(q) \cdot f \tag{2.13}$$

By carrying out the matrix operations, the transformation matrix is obtained as:

$$C_e = \begin{bmatrix} 1 - 2y_q^2 - 2z_q^2 & 2(x_q y_q - w_q z_q) & 2(x_q z_q + w_q y_q) \\ 2(x_q y_q + w_q z_q) & 1 - 2x_q^2 - 2z_q^2 & 2(y_q z_q - w_q x_q) \\ 2(x_q z_q - w_q y_q) & 2(y_q z_q + w_q x_q) & 1 - 2x_q^2 - 2y_q^2 \end{bmatrix} \tag{2.14}$$

Since only the vertical acceleration is of interest in this work, only the third row of the rotation matrix is considered. This results in the complete expression for the acceleration along the Earth frame z-axis as follows:

$$\ddot{z}_e = 2(x_q z_q - w_q y_q)\ddot{x} + 2(y_q z_q + w_q x_q)\ddot{y} + (1 - 2x_q^2 - 2y_q^2)\ddot{z}. \tag{2.15}$$

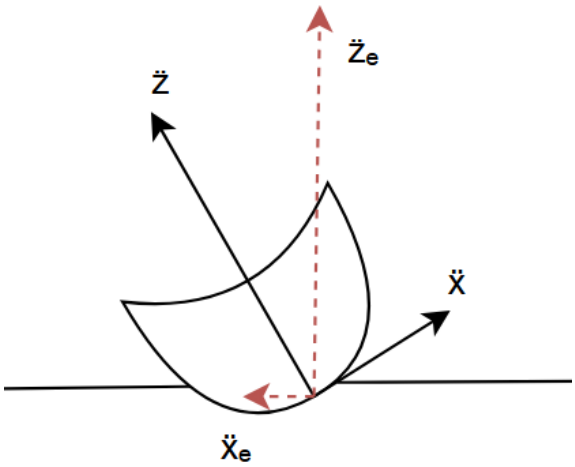

Figure 2.2. Visualisation of coordinate frame transformation

2.8 Discrete Time Systems and Digital Logic

The transition from theoretical control to a real world mechatronic system requires focus on digital timing and multitasking. Real systems face various delays and limited precision, meaning the software must be carefully designed to ensure control logic remains accurate and stable.

2.8.1 Real Time Task Management

In embedded control, multiple processes must often execute seemingly in parallel. A standard operating system may introduce non-deterministic delays. To ensure that a control loop maintains constant sampling period, a real time operating system (RTOS) is used. The core theoretical mechanism is pre-emptive prioritized scheduling, which allows the processor to suspend a low priority task (such as data logging) immediately when a high priority control task requires execution. This reduces sampling jitter, ensuring the mathematical validity of the discrete time regulator. [41]

2.8.2 Data Integrity and Concurrency

When a system utilizes multitasking, different tasks often need to share the same memory resources, such as sensor data or state variables. A Mututal Exclusion (Mutex) is a synchronizations tool used to manage concurrent access. Theoretically, it prevents race conditions which is a timing anomaly that occurs when multiple tasks access shared data concurrently. Mutex ensures that only one thread or task can own the resource at a time. This is critical for data integrity, without it a regulator might read a torn value or a state vector that is only partially updated. [41]

2.8.3 Hardware Timed Pulse Generation

While the fundamental principles of PWM are described in section 2.6, the practical implementation in a multitasking environment introduces the risk of timing instabilities. If the pulses are generated via software, any delay in the processors interrupt handling can cause fluctuations in the duty cycle. To uphold the control precision, the system offloads pulse generation to dedicated hardware timers. This ensures that the high frequency control signals remain decoupled from the main processors execution load, maintaining the deterministic behaviour required for stable flap positioning. [42]

2.9 Composites in Marine Environments

To ensure the durability of the developed system in a marine environment, it is beneficial to understand the material properties as well as the manufacturing methods of the produced components. This because high performance sailing, particularly foiling, subjects parts to substantial dynamic loads and constant exposure to saltwater.

2.9.1 Carbon Fiber

Carbon fiber is a high performance reinforcement material characterized by its high specific strength. In marine engineering, these properties are critical for maintaining structural integrity under the high hydrodynamic loads experienced during foiling. [43]

According to Jones [43], one of the most significant advantages of carbon fiber is its excellent resistance to the harsh marine environment. Unlike traditional metallic materials, carbon fiber reinforced polymers are do not suffer from oxidation and show high resistance to environmental degradation caused by constant exposure to saltwater and UV radiation. Furthermore, carbon fiber composites exhibit high fatigue resistance, which could prove essential for the components manufactured in this project.

2.9.2 Flax Fiber

To address the environmental impact of composite manufacturing, natural fibers such as flax have emerged as an alternative to synthetic reinforcements. Flax fibers are renewable and require significantly less energy to produce compared to carbon fiber. Research on bio-based composites show that flax fibers offer comparable specific stiffness and inherent vibration damping properties, which can reduce structural noise and fatigue in sailing components. [44]

Flax fibers alone may not match the absolute tensile strength of carbon fiber. However, the use of a hybrid combining flax with carbon fiber allows for a more environmentally friendly alternative. This hybridization strategy enhances the balance between mechanical performance and sustainability. Flax fibers contribute to a more resilient structure that can absorb impacts more effectively than pure carbon fiber laminates, while the carbon fiber provides the necessary structural rigidity.

2.9.3 Lamination and Forged Fiber manufacturing

The mechanical properties of a composite part are dependent on the orientation and continuity of the fibers within the part, which is determined during manufacturing. Continuous fiber lamination involves layering whole sheets of reinforcement, which allows loads to be distributed along the unbroken fibers for maximum stiffness and strength. When combined with compression moulding, this process effectively removes entrapped air as well as excess epoxy and ensures a high fiber to resin ratio. [45]

In contrast, forged fiber composites utilize short cut, discontinuous fibers that can flow more easily into complex geometries and tight pockets where continuous sheets would wrinkle. While this method offers high dimensional accuracy for complex parts, the lack of fiber continuity generally results in lower tensile strength compared to traditional laminates. This creates a trade off between the absolute structural capacity of lamination and the geometric precision of the forged process. [45]

3

Methods

In this chapter, the methodology for this project is presented. The first step of the process was the construction of a miniature system which then transitioned to the development of the control system applied to *Saga*. Thereafter, the mechatronic system design will be presented with the sourced components, electronic circuit and hardware housing and assembly. Following this, the modelling and simulations conducted is presented, as well as the software design, data collection, and finally, system test and evaluation.

3.1 Construction of a Miniature System

In the initial phase of the project, prior to component selection and procurement for the full-scale system, a small-scale prototype was developed. The purpose of this model was to provide a portable platform for demonstrations, to support software development and testing, and to visualise system behaviour in response to sensor inputs.

The prototype was constructed using components already available within the project group. The system was based on an ESP32 development board, powered by a USB power bank to ensure portability.

For angle sensing of the model wand, a potentiometer was used. This acted as a variable voltage divider, which created a DC voltage that depended linearly on the angle of the wand. This voltage could then be read by the on board ADC of the ESP32.

A simple IMU was also used to provide angle and acceleration data to the MCU. The IMU, like many development board, supports the digital I^2C protocol to relay data to MCU´s. I^2C was therefore used to allow the MCU to read the data from the IMU.

For actuation of the model hydrofoil flap, a small servo motor was used. A series of mechanical components were modeled in CAD and manufactured using FDM print-

ers. From the available filaments, PLA (Polylactic Acid) plastic for its favourable printing characteristics, allowing for stiff parts with few defects. The printed components were then assembled into a miniature illustrating the system. A drawing of the miniature, based on a CAD assembly of the printed components, can be seen in Figure 3.1.

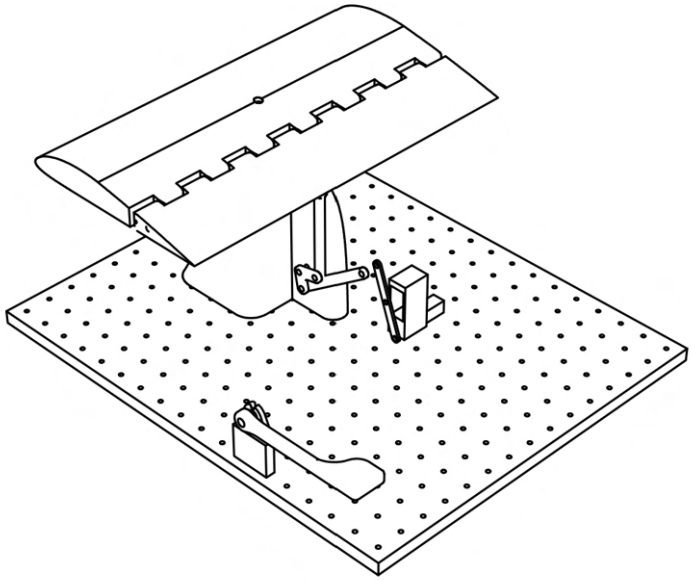

Figure 3.1. Isometric drawing of the miniature model.

3.2 Mechatronic System Design

The mechatronic system can be broken down into multiple sub systems for sensing, computing and actuation respectively. Since the Moth dinghy *Saga* is an already built boat, there were some constraints to take into account regarding the mechatronic system design. Wished by CFSail was that there would be no major changes to the vessel and that the changes made would be modular.

The electronic architecture of the control system, illustrated in Figure 3.2, was designed to acquire sensor data, process control algorithms in real time and drive the mechanical actuator. Component selection was guided by the physical constraints and harsh operating conditions of the Moth dinghy, with requirements for waterproofing and mechanical robustness to ensure reliable operation in a marine environment. The following sections describe the hardware components forming the mechatronic system.

3.2.1 Analogue to Digital Converter (ADC)

For reading of analogue voltages, such as output voltages from sensors (see 3.2.4), sampling and quantization of the signal is performed with a Texas Instruments ASD1115-based board. This was partially due to availability and low cost, but

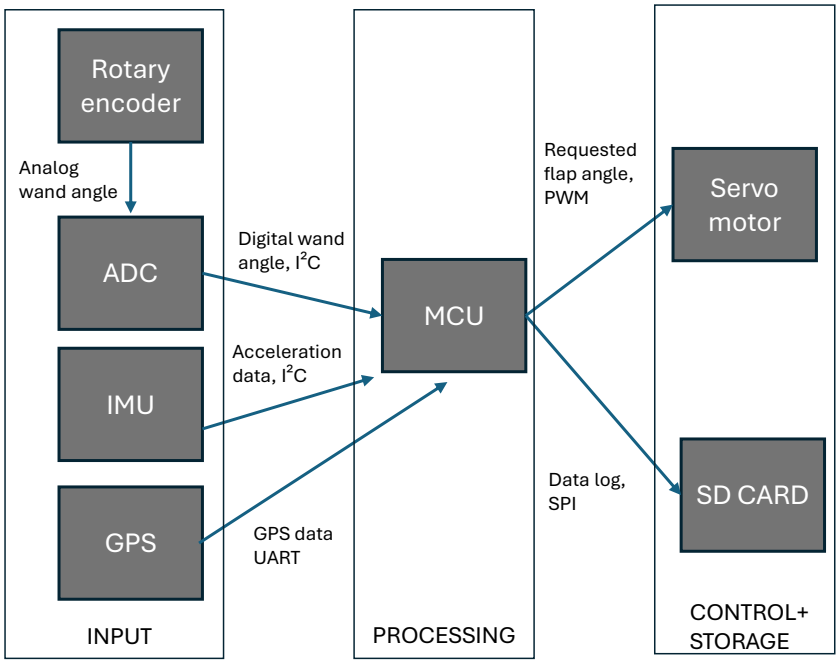

Figure 3.2. Block diagram describing data flow in the mechatronic system.

also because its performance was deemed sufficient for the task. The ASD1115 features 16 bit resolution, with a sample rate of up to 860 samples per second according to its data sheet. ASD1115 also features an interface I^2C that allows simple communications with the MCU.

3.2.2 Battery

A battery is needed to power the system. To comply with safety rules at the Department of Electrical engineering for electronics built for wet environments, DC voltages cannot exceed 15 V. Packaging and power density is prioritized, as a compact end system is preferred. A 3S LiPo (3 cells in series Lithium-Polymer) battery was chosen as the power source. The selected unit has a capacity of 2.4 Ah at 11.1 V, resulting in a nominal energy of 26.6 Wh. With a maximum discharge rate of 20 C, giving us a maximum current of 48 A, it can supply enough current for the servo actuator. The battery does, however, lack built in protection in case of a short circuit or similar failures of the electrical system. Therefore, a 15 A automotive fuse is added in line with the battery, ensuring the battery will be disconnected in case of a short circuit. See Figure B.2.

3.2.3 Servo Motor

Several actuator types were considered, and a hobby-grade servo was selected due to its compact size, low cost, integrated control electronics, and high torque capability. The selected model, DS51150-12V, provides up to 173, kg cm torque and a nominal travel range of 180°. The servo was modified to improve water resistance by sealing electronic components with epoxy, applying sealant to joints, filling the housing with

silicone grease, and adding an additional O-ring to the gearbox.

3.2.4 Angle Sensor

To measure the angle difference of the wand, an RFD-4000 rotary sensor from Novotechnik was chosen. It is a magnetic absolute encoder relying on the Hall effect explained in 2.5, to measure the angle of an externally mounted magnet. The output signal is an analogue voltage output ratio-metric representing the angle. As it is an analogue signal, an analogue to digital converter was necessary to be applicable with the other digital components. The system consists of two physically independent components: a stationary unit containing the sensing electronic and a separate magnet attached to the rotating shaft. As shaft rotates, the orientation of the magnetic field changes. The sensor detects this shift and provides an analogue voltage output ratio-metric to the supply voltage, where the voltage level directly represents the specific angle of the shaft. Internal sampling electronics convert magnetic data into a precise signal with 12-bit resolution and an independent linearity of $\pm 5\%$, which ensures a consistent relation between the physical wand angle and the voltage output.

There are multiple reasons as to why this sensor is suitable for this application. The contactless operation of the sensor makes precise shaft alignments and sealing unneccesary, allowing for a lateral offset of ± 3mm. It is also falls under protection class IP69 which makes it water proof up until 8 MPa making it suitable for the intended environment.

3.2.5 Inertial Measurement Unit

The BNO085 (CEVA/Hillcrest Labs) was selected as the IMU for the mechatronic system, the choice was driven by the need to address the computational limitations of the MCU. While the theoretical foundations of state estimation, including Kalman filter are essential for stable flight, the implementation is computationally demanding. The BNO085 features an integrated processor that runs software to perform high frequency sensor fusion internally.

This approach provides a significant advantage, by utilizing a built in Extended Kalman Filter (see Section 2.3.4) to handle complex quaternion based rotation and drift compensation mathematics. By delegating these matrix-heavy tasks to the IMU the MCU is not burdened with simultaneous sensor fusion and regulation tasks, thereby enabling the system to maintain the high frequency, deterministic timing required for stable control.

3.2.6 GPS Module

To provide an absolute temporal and spatial reference, a NEO-6M GPS module was selected and integrated into the system. The primary selection criterion was the need for a reliable universal time coordinated (UTC) unit to establish a time anchor between the log data and real world. Additionally the module's ability to track

speed over ground (SOG) provides essential context for evaluating the controllers performance at different boat speeds.

3.2.7 Microcontroller

The ESP32-Dev-30P microcontroller was selected as the central processing unit of the system, primarily due to its balance between cost and computational performance.

The microcontroller's peripheral set covers all communication protocols required by the system: I^2C, SPI, UART. A diagram of how the aforementioned protocols are used to interface with other components can be seen in Figure 3.2.

The built-in support for FreeRTOS further enabled the implementation of concurrent execution of the control loop, sensor sampling, and data logging as separate prioritized tasks. This multitasking capability ensures that the high-priority control loop can operate deterministically without being interrupted by lower-priority background processes such as file writing.

3.3 Electronic Circuit

The electronic circuitry was developed through iteration over the course of the project. Early circuits were assembled on breadboard, which provided flexibility and quick assembly to test early firmwares and communication types between components, such as I^2C, UART and SPI. This method functioned well for small systems with few connections and components, however when trying to incorporate multiple communication buses and components, the limited robustness of breadboards caused issues with loose connections, broken lanes, and connections coming undone during transport.

In later stages of the projects, the circuit design was finalized (see fig. B.2) and transferred to prototype PCBs and connected using point to point soldering. This method was chosen because it provides flexibility if quick modifications and additions are needed, similar to breadboards, but with robustness resembling that of custom circuit boards. The prototype PCB´s can be seen assembled in a waterproof housing in Figure 3.14a.

3.4 Hardware Housing and Assembly

Although the project is based on an existing boat and control system, some provisions for the mechatronic system were necessary. The need for these changes stems from the difference in the way the wand transmits outputs and the challenges of integrating sensitive electronics into a harsh saltwater environment. These modifications were implemented to facilitate the integration of electronic components into the existing system.

The modifications are categorized into three primary areas: the wand attachment, where the angle/angular sensor is integrated; the wing attachment area, which houses the waterproof electronics enclosure; and the section above the hydrofoil, where the servo actuator is positioned to control the flap. These areas can be seen illustrated in Figure 3.3. Ultimately these changes means that the linkarm between the wand and bellcrank illustrated in Figure 1.9 could be removed, as it is replaced by electrical cabling between the sensor at the wand and the waterproof box.

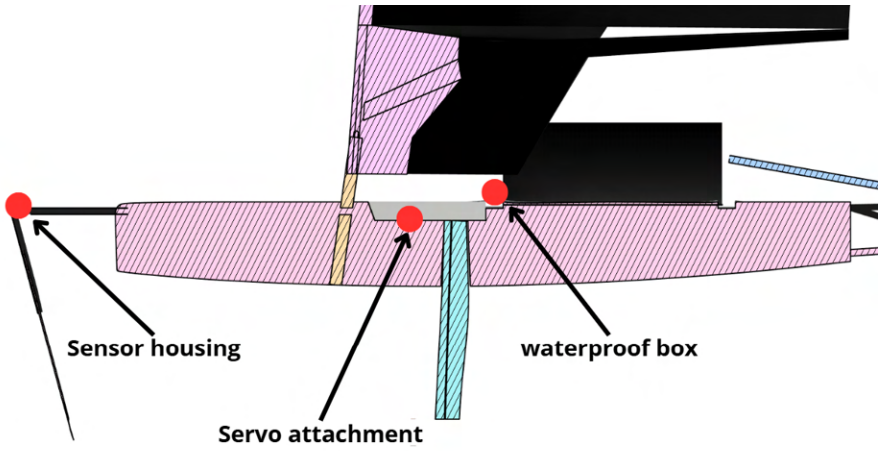

Figure 3.3. Areas of physical modification

3.4.1 Sensor Housing and New Wand

To physically integrate the rotary sensor described in 3.2.4 at the centre of rotation of the wand, a new mounting solution for the wand was required, as the existing wand mount was deemed unfit for the task. The reason for this is the need for near concentricity (within a few mm) between the sensor and magnet. Existing wand mount could not ensure said concentricity.

There are some challenges in transforming this part of the boat. In its existing form this part is simple and exposed. It is also designed to be able to swing a bit from side to side in order to slide along the hull when it is fully folded. This could not be allowed when using the chosen sensor. Further challenges are the need for sensor and magnet concentricity. It is also important that this part is rugged enough to withstand the forces which a crash dive at 25 knots from over 1 metre of height would cause.

In modern Moth dinghies the wand attachment is designed as seen in Figure 3.4 with closed top and open bottom. This design served as an inspiration and starting point for the development of the new part.

Figure 3.4. Wand attachment on a production Moth dinghy, as seen from below.

The developed assembly, illustrated in Figure 3.5, utilizes specific dimensions and tolerances to ensure that the encoder accurately reads the position of the wand.

Figure 3.5. Exploded view of the sensor housing and wand assembly. From left to right: wand housing, wand, magnet attachment, and sensor housing with wall fitting for the encoder.

With correct measurements and functionality of the component ready, the geometry of the housing was redesigned for both mechanical clearance and structural integration. The internal ceiling of the housing was elevated to accommodate a greater lever range for the wand, ensuring unobstructed movement during operation. Additionally, a beam was integrated to the rear of the component to provide a secure mounting point to the bowsprit on the boat. The final design, which incorporates a refined profile for improved aesthetics, is illustrated in Figure 3.6.

Figure 3.6. Rendering of final version

As mentioned, the wand in its current form is allowed to flex a bit to avoid breaking when hitting the hull. As the sensor doesn't allow any movement of that kind there was also need for a new wand solution. This was done by designing a new wand with an offset angle of 5 degrees from the center of the boat, which can be seen in Figure 3.13. Drawings of the components can be found in Appendix B.4 - B.9.

Manufacturing of Sensor Housing and Wand

The sensor housing and wand attachment are located at the bow of the boat, an exposed position that requires a durable construction to handle operational stress and impact forces. To meet these requirements, carbon fiber was selected as the primary material. Its high structural stiffness, light weight and common use in competitive sailing make it ideal for the high performance demands of the SuMoth Challenge (see Section 2.9.1). Furthermore, the material is capable of withstanding the harsh marine environment without corroding, ensuring long term structural integrity.

To align with the sustainability goals of the SuMoth Challenge, a hybrid composite strategy was adopted. By integrating flax fibers with the carbon fiber, the construction benefits from the high stiffness of carbon while utilizing the renewable properties of the natural fibers (see Section 2.9.2).

For time and simplicity reasons, it was decided that only the wand and the wand housing being connected to the boat would be manufactured from carbon fiber and flax fiber while the other half housing the sensor would be 3D printed in PETG. All manufacturing processes involving fiber reinforcement and epoxy resins were carried out at the CFSail off campus workshop in Mölnlycke.

The parts were manufactured in a similar way where the first step of the process was to design moulds and 3D print them. The filament chosen for the moulds was PETG due to its higher temperature resistance, allowing it to withstand the heat generated during the curing process. The moulds can be seen in Figure 3.7

(a) Mould for the housing half

(b) Mould for the wand

Figure 3.7. 3D printed moulds

The moulds were sanded and treated with a release agent to prevent the parts from sticking, and then packed with fiber and epoxy resin. Two different methods were used depending on the geometry of the components.

The outer layers of the housing half were produced by hand lay-up or lamination, where continuous fiber sheets were saturated with epoxy resin and placed carefully in the mould to ensure a flat and uniform surface finish. In contrast, the beam and the wand were produced using a method where the fibers were cut and mixed into a *dough* with the epoxy, called a forged carbon process. (see Section 2.9.3)

The processes seen in Figure 3.8 involves a combination of carbon fiber and flax together with epoxy resin and hardener. The fibers are thoroughly soaked in epoxy and then, as shown in Figure 3.9, compressed in the mould for at least 24 hours to fully cure before being broken out of the mould.

(a) Lamination of housing

(b) Forging of the wand

Figure 3.8. Lamination and forging of fibers

(a) The closed mould of the housing

(b) The closed mould of the wand

Figure 3.9. Closed moulds

Figure 3.10 shows the parts after being removed from the moulds. After this the parts were ground, clear-coated, and assembled.

(a) Housing broken out of the mould

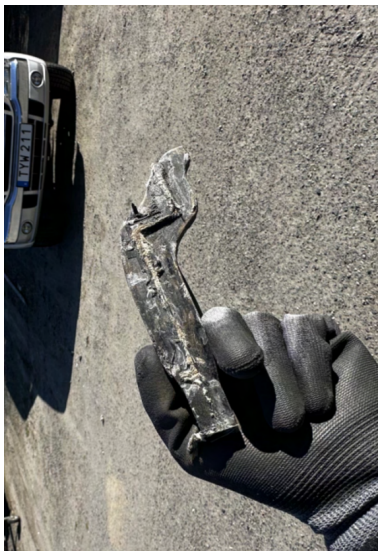

(b) Wand broken out of the mould

Figure 3.10. Parts fresh from the moulds

As shown in Figure 3.11, the wand component was bonded to a repurposed floorball stick made of carbon fiber, while the housing part was glued to a flat carbon fiber plate serving as the central wall of the construction. The reuse of discarded carbon fiber products, such as floorball and hockey sticks, is a fundamental strategy for CFSail. This approach is both a durable and environmentally sustainable method of producing high quality components, directly aligning with the ecological goals of the SuMoth Challenge.

(a) Housing glued to central wall

(b) Wand bonded with floorball stick

Figure 3.11. Post processing of parts

The half of the housing holding the sensor, along with the magnet holder, were

designed using CAD and subsequently 3D printed in PETG. The composite fiber parts and the 3D-printed components were then assembled into a single integrated unit as seen in 3.12 and mounted on *Saga* in Figure 3.13.

(a) Wand and housing assembled

(b) Assembled housing seen from below

Figure 3.12. Pictures detailing the wand mechanism assembled.

As the testing phase approached, time constraints meant that functional performance had to be prioritized over the visual finish. Because of this, some parts were left with a rougher surface and the bolts used were available alternatives rather than the ideal ones. Despite these aesthetic compromises, the assembly was fully operational and performed as intended during the initial fittings.

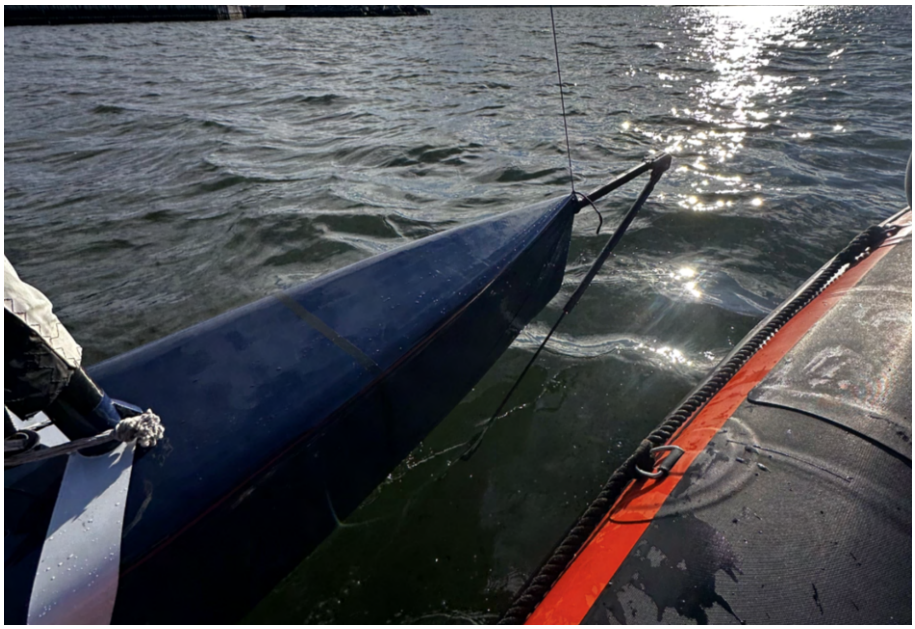

Figure 3.13. The wand clears the hull in testing, as intended

3.4.2 Waterproof Box

The electronic components mentioned in section 3.2 were fitted in a waterproof box with internal dimensions of 160x85 mm. An insert was designed and 3D printed to hold all the electronic components but the encoder and servo motor. The insert allows for stable and controlled placement in the box, ensuring protection from internal shocks created by external forces. The design allows for easy accessibility to the SD-card, microcontrollers USB-C port and the battery while testing. The box and the 3D printed insert can be seen in Figure 3.14

(a) Electrical components in the waterproof box

(b) Empty insert

Figure 3.14. Waterproof box and 3D printed insert

Since the Moth dinghy has a small hull and frequently submerges, the system is designed to withstand full submersion. The box is rated as IP68 ensuring protection against continuous immersion in water and has a hard plastic polypropylene shell to withstand impacts.

To mount the box without interfering with vital mechanisms, such as the sail or deck lines, a custom attachment was developed. This attachment was made of a wooden plank and was placed in the central part of the boat, secured using the same attachments as the wings. A strap was then used to easily be able to fix and remove the box from the plank. To be able to connect the sensor and servo located outside the box with the electronics inside, two M12 cable connectors were installed in the sidewall of the box. These were fitted with o-rings and reinforced with sealant to ensure waterproofing of the box. Additionally, for safety reasons an emergency stop was implemented in the form of a classic dead man's switch, which is a standard safety mechanism in marine applications. The box fitted to the boat can be seen in Figure 3.15.

Figure 3.15. Waterproof box secured on board Saga

3.4.3 Servo Fitting and Flap Actuation

In the purely mechanical system originally mounted on the Moth dinghy, the flap is actuated by the wand through a series of linkages as explained in Figure 1.10. The ideal servo location based on packaging and linkage alignment was determined

to be slightly forward of the foil mast attachment point. This allows the servo to actuate the existing bell crank mounted on the top of the foil mast through a short connecting rod, which in turn acts on the flap through a pushrod mounted in the foil mast. A section view of the servo mounting arrangement can be seen in Figure 3.16.

To mount the servo to the hull, an existing carbon plate with tapped holes, glued near the intended position of the servo, could be used. An adaptor bracket to mount the servo to the plate was designed in CAD, and manufactured using FDM. PETG filament was chosen for its high toughness and impact resistance, which was seen as beneficial to withstand the dynamic loading produced by the servo. A drawing of this component can be seen in Figure B.3.

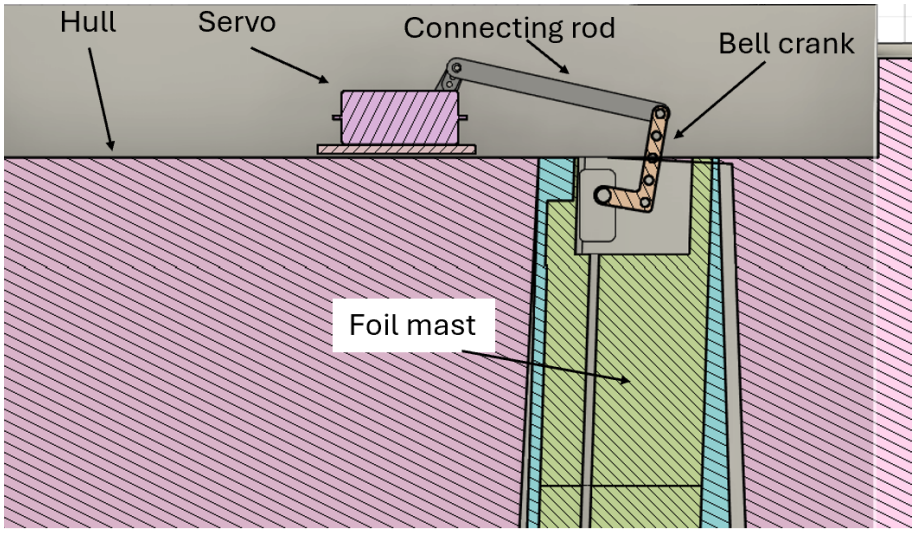

Figure 3.16. Section view of servo mounting arrangment, from CAD mockups

Motion analysis in the CAD model, together with physical measurements on the existing mechatronic system, was used to define the allowable movement range of the servo. Overextension of the flap could potentially cause mechanical damage, so hard limits for the servo travel were implemented in software. The maximum allowable flap deflection was specified by CFSail as $\pm 9°$. By manually actuating the bell crank, recording the corresponding flap deflection, and measuring the servo horn length, the maximum allowable servo travel was calculated. Assuming a locally linear relation between servo rotation and flap deflection, this was estimated as:

$$\alpha_{\max} = \frac{\alpha_{\text{meas}}}{\delta_{\text{meas}}} \delta_{\max} \tag{3.1}$$

Where α is the servo angle and δ the flap angle. Using the measured linkage ratio and the specified limit $\theta_{\text{flap,max}} = 8°$, the allowable servo travel was determined to be $\pm 28°$.

3.5 Simulation

A major challenge during the project was the limited availability of real world testing. The development of the physical system was expected to be both iterative and time consuming, making on water testing feasible only during the later stages of the project. Furthermore, real world testing required several resources, including a sufficient number of personnel, favourable weather conditions, and access to an experienced sailor capable of operating the boat safely. As a consequence of the limited testing opportunities, an initial controller design with preliminary tuning parameters was required before the first field tests.

A PID-based control strategy was considered suitable for the project since it does not require an accurate mathematical model of the system, as described in section 1.3. This was beneficial due to the limited availability of real world testing data, as described in section 1.3

To support controller development, a simulation environment based on a linearized model of the boat dynamics around a nominal foiling operating point was implemented. The purpose of the simulation was to evaluate the proposed control strategy and obtain initial controller tuning parameters prior to experimental testing.

3.5.1 Numeric System Model

In order to model the dynamics of the boat, several system parameters must be determined or estimated. The values presented in Table 3.1 were provided by CFSail based on their own simulation work [46]. The intended operating speed of the vessel is approximately 25 knots, corresponding to $v = 12.9\,\mathrm{m/s}$ in SI-units. At this operating point, the rudder foil is assumed not to generate any vertical lift. Consequently, the entire lifting force is produced by the main foil.

Table 3.1. Estimated values for the operating point variables.

Variable	Estimated value
m	$128\,\mathrm{kg}$
S	$0.0776\,\mathrm{m}^2$
ρ	$1000\,\mathrm{kg\,m}^{-3}$
C_{L0}	0.75
$C_{L\theta}$	$6.15\,\mathrm{rad}^{-1}$
$C_{L\delta}$	$4.2\,\mathrm{rad}^{-1}$
v_0	$12.9\,\mathrm{m/s}$
θ_0	$0\,\mathrm{rad}$
δ_0	$-0.132\,\mathrm{rad}$

Here, the mass m is estimated including the sailor. Further, the density, ρ is assuming fresh water, as the main competition will be conducted in fresh water. Some

tests were made in salt water, however, the difference in density is considered negligible to the results of the simulation. With these values, the lift force equation 2.4, can be numerically estimated as follows:

$$L = 38.8v^2(0.75 + 6.15\theta + 4.2\delta) \tag{3.2}$$

This equation combined with the values at the operating point allowed the derivation of $\delta_0 = -0.132$ radians. The system was then linearized in accordance of the method explained in section 2.2, resulting in a system model for vertical acceleration as follows:

$$\ddot{z} = a \cdot (C_{L\alpha} \cdot (\theta - \theta_0) + C_{L\delta} \cdot (\delta - \delta_0)) + b \cdot (v - v_0) \tag{3.3}$$

Here, a and b are constants derived from first order taylor expansion around the operating point, evaluated to:

$$a = \frac{1}{2m}\rho v_0^2 S \tag{3.4}$$

$$b = \frac{1}{m}\rho v_0 S(C_{L0} + C_{L\theta}\theta_0 + C_{L\delta}\delta_0) \tag{3.5}$$

.

Further, the numerical system model is evaluated as follows:

$$\ddot{z} = 310 \cdot (\theta - \theta_0) + 212 \cdot (\delta - \delta_0) + 1.53 \cdot (v - v_0) \tag{3.6}$$

The theoretical model of the system only takes the lift force from the foil into account, disregarding external hydrodynamical damping forces. To obtain a more realistic system response, a damping force F_d was introduced as follows:

$$F_d = C_d\dot{z} \tag{3.7}$$

Where $\dot{z}$ is the vertical velocity and $C_d = 3$ is an empirically chosen damping constant. The damping coefficient was not based on hydrodynamical experimental data, but rather selected through iterative simulation and chosen to obtain a qualitatively reasonable response.

Figure 3.17 illustrates the simulated vertical response following a step change in flap angle δ, comparing the damped and undamped models in open-loop simulation.

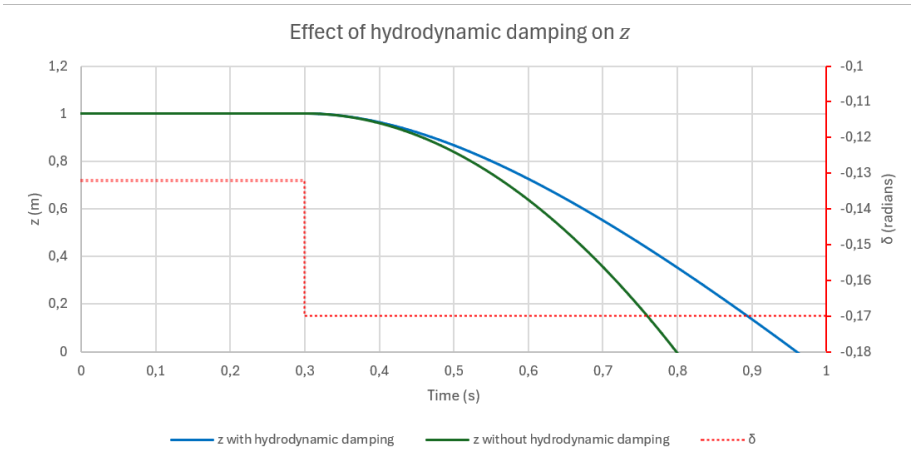

Figure 3.17. Comparison of the ride height response z with and without hydrodynamic damping for a step change in flap angle δ.

3.5.2 Frequency Analysis of Disturbance

To estimate the dominant oscillation frequency of the vessel during foiling, needed for the simulation, high resolution videos of the boat equipped with the current mechanical control system was analysed. The observed oscillatory motion consisted of both the vessel's vertical movement and wave-induced disturbances. By counting the number of recurring oscillation and wand deflection events over a known time interval, an estimate of the effective system frequency could be obtained. Since the measured oscillation was assumed to be partly caused by wave induced excitation, the estimated frequency was used as an approximation of the dominant wave disturbance frequency in the simulation. The wave disturbance was therefore modelled as a periodic input with this frequency, allowing the controller to be evaluated under conditions similar to those observed during testing.

The result from this experiment is presented in Table 3.2.

Table 3.2. Number of deflection events during a time period

Test nr	Deflection events	Duration (s)	Frequency (Hz)
1	36	7	5.1
2	30	8	3.8
3	28	6	4.7

Resulting in an average frequency of $f = 4.5Hz$.

3.5.3 Filter

Since the wand measures the instantaneous distance to the water surface, the measurement does not directly represent the absolute ride height in a global reference frame. Instead, the signal is strongly influenced by local surface variations caused by waves and splashing.

The objective of the control system is not to follow these short term surface variations, but rather to maintain a stable ride height relative to the mean water level. Consequently, rapid fluctuations in the wand measurement may lead to unnecessary actuator activity and unstable control behaviour without representing meaningful changes in the vessel ride height.

To reduce the controller sensitivity to such high frequency surface disturbances, a low-pass filter was introduced in the wand measurement signal. The purpose of the filter was therefore not to suppress the physical motion of the vessel itself, but rather to reduce the influence of short term wave induced variations on the ride height estimation.

Based on the frequency analysis results in 3.5.2, the average wave induced disturbance frequency was estimated to be 4.5 Hz. By identifying this specific frequency, the filter was tuned to suppress the noise originating from the water surface while maintaining the necessary bandwidth for the primary control loop to respond to the actual vertical dynamics of the boat.

3.5.4 Simulink

The complete linearized model was implemented in Simulink, where multiple subsystems representing the different parts of the control system were constructed. Further details and schematic representations of these subsystems can be found in Appendix A.1.

Instead of relying on built-in Simulink controller and filter blocks, the PID regulator and filtering algorithms were implemented manually. This approach allowed the algorithms to be directly translated and verified in code, ensuring consistency between the simulation environment and the embedded software implementation. The block scheme of the simulation is presented in Figure 3.18.

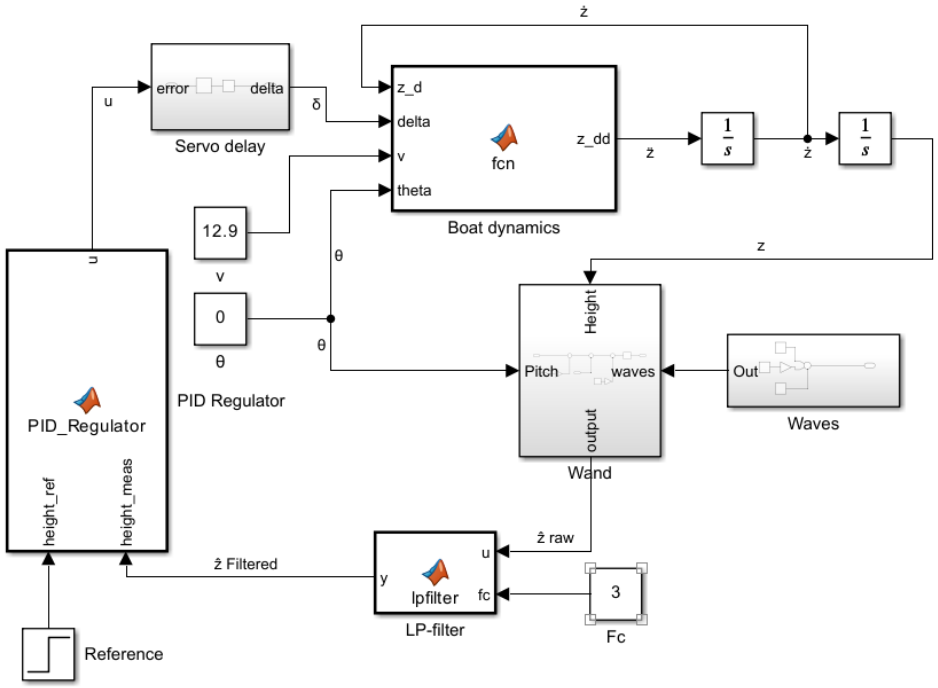

Figure 3.18. Simulink block diagram

3.5.5 Simulation Results

During sailing, the unpredictable nature of the wind can cause sudden changes in the vessels behaviour. Robustness against disturbances is therefore crucial to ensure stable ride height.

Figure 3.19 shows the simulated response of the PID-controlled system to a step change in velocity from $v = 12.9\,\mathrm{m/s}$ to $v = 11\,\mathrm{m/s}$, introduced as a disturbance. As the velocity deviates from the operating point, the generated lift force decreases, causing the vessel to temporarily fall below the reference ride height. Through the integral action of the controller, the system compensates for the disturbance and returns to the desired ride height after the transient response.

As the wand is placed at the bow of the vessel, a negative change in pitch causes the bow to decrease its height relative the surface. This causes the estimated height from the wand to be inconsistent with the ride height of the foil, placed in the centre of the boat. This behaviour is simulated linearly, assuming small pitch angles, as follows:

$$\hat{z}_w = \hat{z}_c + l\theta \tag{3.8}$$

Where $\hat{z}_c$ and $\hat{z}_w$ is the estimated height at the centre of the boat and the estimated height at the wand attachment point respectively. Further, l is the length from the

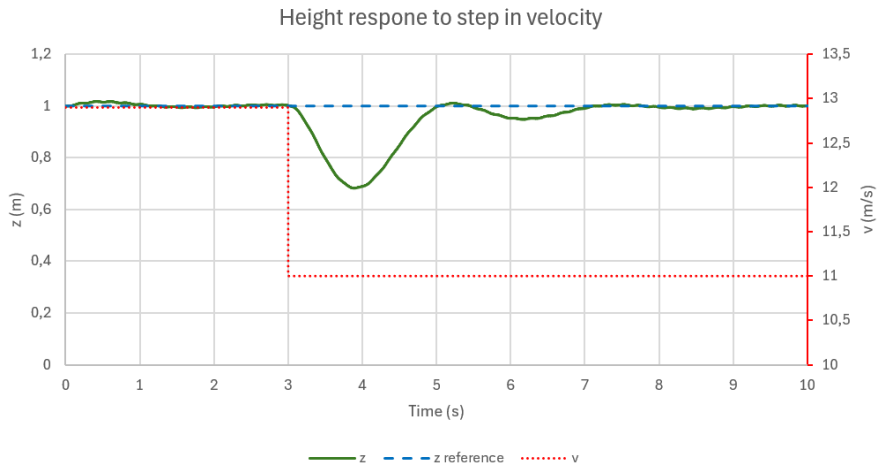

Figure 3.19. Response to a step change in velocity

centre to the attachment of the wand. θ is the pitch angle, given that $sin(\theta) \approx \theta$ for small angles.

To investigate whether a more representative estimate of the vessel ride height could improve the control performance, the pitch angle measured by the IMU was used to compensate for the longitudinal offset between the wand and the vessel centre. This was simulated by subtracting the correction added in equation 3.8, resulting in $\hat{z}_c = \hat{z}_w$.

Figure 3.20 shows the response of the uncompensated and pitch compensated height estimates to a step change in pitch angle.

The pitch compensated estimate exhibits a slightly slower response compared to the uncompensated measurement. Although the compensated signal provides a geometrically more accurate estimate of the vessel centre height, part of the anticipatory behaviour naturally introduced by the forward-mounted wand is removed. As a result, the controller reacts less aggressively to pitching disturbances, leading to a somewhat less responsive system under the simulated conditions. The uncompensated measurement therefore provided a more favourable control response in this case.

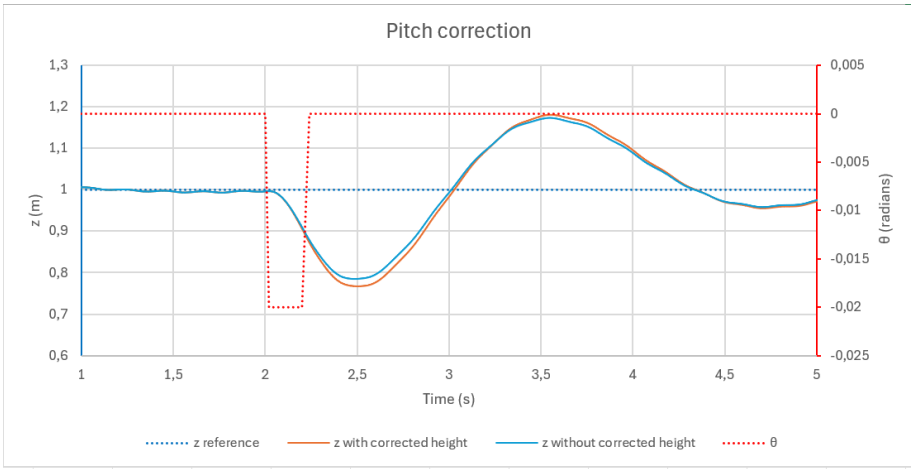

Figure 3.20. Response to a step change in pitch angle

Figure 3.21 shows the closed-loop response to a step change in the reference ride height from 1.0m to 0.7m. The controller is able to track the new reference value and stabilise around the desired height after the transient response. The response exhibits noticeable overshoot and damped oscillatory behaviour before converging to the reference value. No significant steady-state error can be observed once the transient has settled.

While the transient overshoot is larger than desired, it was considered acceptable in order to achieve faster reference tracking. Less aggressive controller tuning reduced the overshoot, but resulted in a significantly slower system response.

Figure 3.22 shows the flap angle ,δ, during the same reference step. While the allowable flap angle range is between $\delta = -0.17$ radians and $\delta = 0.17$ radians, the simulation only uses angles between approximately $\delta = -0.155$ radians and $\delta = -0.115$ radians. Despite using only a limited portion of the available range, the flap deflections are sufficient to produce a clear response in the vessel ride height.

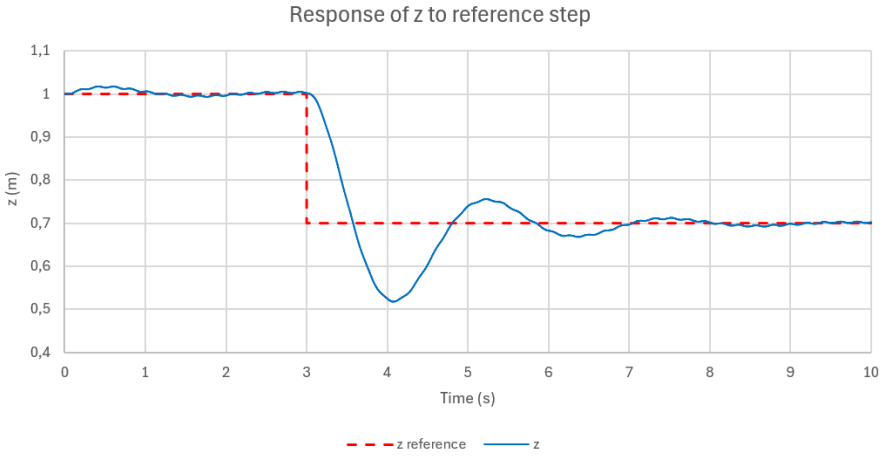

Figure 3.21. Closed loop response to a step change in reference ride height

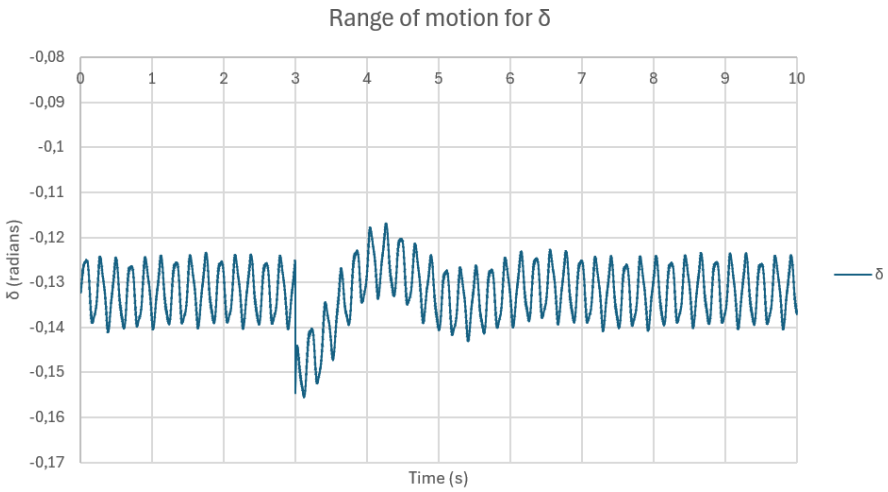

Figure 3.22. Flap angle associated with step response in figure

Based on the simulated responses presented above, a set of regulator parameters was selected to provide a compromise between response speed, oscillatory behaviour and steady-state accuracy. These are presented in Table 3.3.

Table 3.3. Selected PID regulator parameters

Variable	Value
k_p	0.05
k_i	0.004
k_d	0.005

3.6 Software Design

This section describes the process of developing the software used in the project. It includes code and architecture relevant for the final system.

3.6.1 Parallel Programming

To facilitate data logging and real time monitoring without interfering with the control loop, concurrent programming principles were introduced using FreeRTOS. Different functionalities of the system were separated into FreeRTOS tasks, operating similarly to threads. Thread safety is guaranteed with mutexes, semaphores, and queues provided by FreeRTOS, ensuring safe access to shared resources. This architecture allowed for task prioritization, enabling the control loop to have a higher priority than background tasks, such as data logging. This ensured deterministic timing for the control system while maintaining continuous sensor sampling and SD-card logging.

3.6.2 Ride Height Control Code Implementation

The control system implementation is done in C programming language. Using the ESP-IDF framework and utilizing the FreeRTOS (real time operating system) to achieve a deterministic schedule.

The process begins in a dedicated sensor task that reads analogue measurements from the magnetic encoder via the ADC module. This raw data is converted into an angle and dispatched to a control task, which serves as the system's central processing unit. Here, trigonometric calculations are performed to estimate the boat's current ride height.

To manage the inevitable disturbances in ride height due to measuring the water surface, a digital low-pass filter in the form of an Exponential moving average (EMA), explained in section 2.3.3 is applied to the height signal before it reaches the regulator with a smoothing factor of $\alpha = 0.1$

The core of the control loop consists of a PID regulator that calculates the necessary flap deflection based on the error between the measured ride height and the set-point. To ensure the structural integrity of the hydrofoil, the control software saturates the output to $\pm 8.64°$. While the servo is mechanically capable of a wider range of motion, this software-defined fail-safe ensures that the flap operates within its physical structural limits, which prevents the servo from overstressing it, and breaking the foil.

However, imposing such constraints introduces a risk of integrator windup described in 2.3.2 To mitigate this, anti-windup logic was implemented, deactivating the integration process during large errors, specifically when the height error exceeds a threshold of 0.1m, which symbolises 11% deviation from the 0.9m ride height. This ensures the system remains responsive and avoids the significance overshoots that would otherwise occur when the vessel returns to its controllable range.

To enhance the stability of the PID regulator and prevent erratic flap movements caused by derivative kick or high frequency sensor noise, a second EMA-filter was applied to the derivative term. The raw derivative values is passed through the EMA-filter before being used in the final control output calculation. A smoothing factor of $\alpha = 0.05$ was selected for this implementation.

Finally, interaction with the actuator is handled via the processors LEDC peripheral. By allowing the hardware to generate the PWM described in 2.6, timing deviations caused by the software interrupts are eliminated, which gives a deterministic and responsive regulation of the flap position.

A visual representation of the software architecture is presented in Figure 3.23.

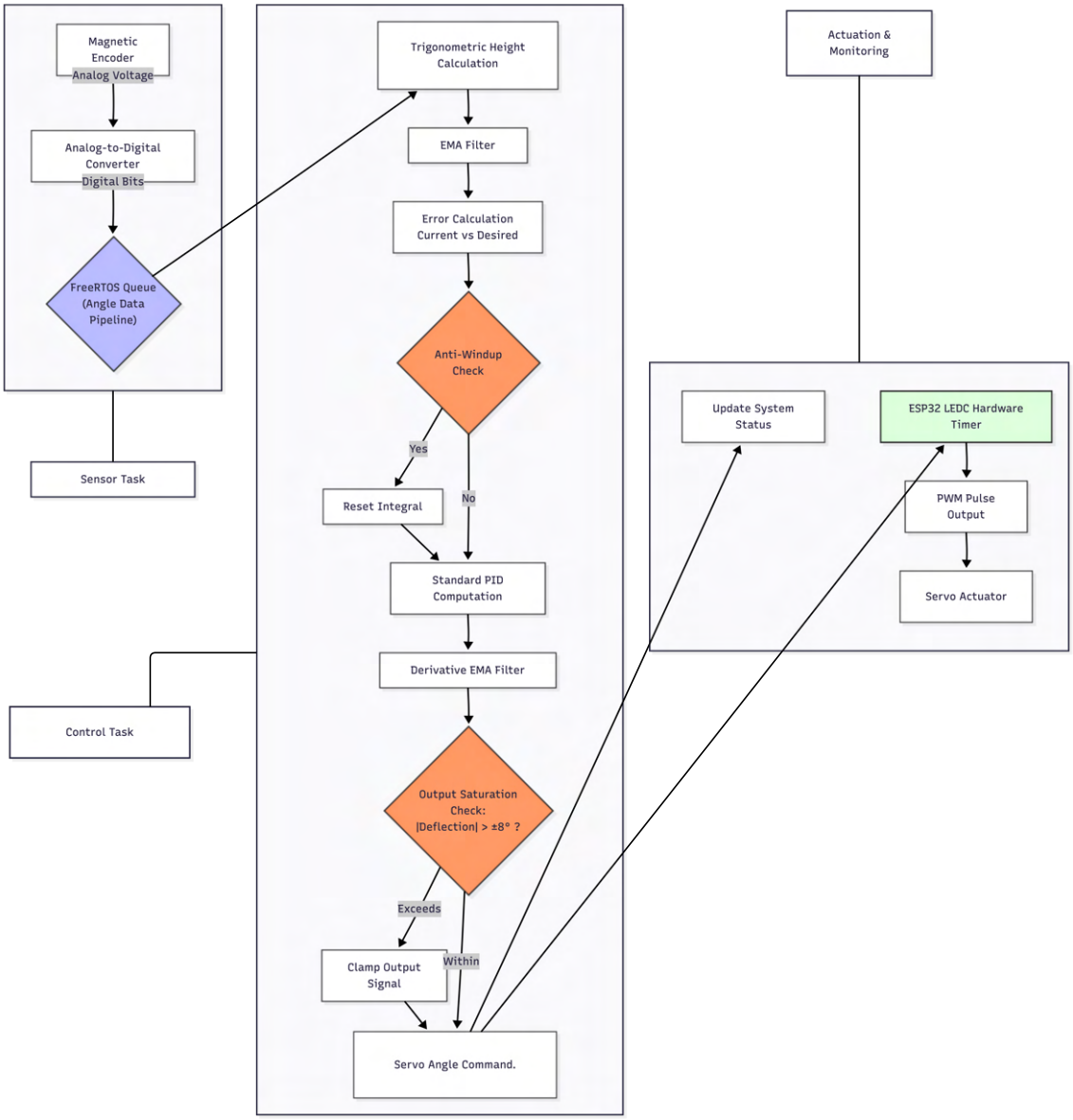

Figure 3.23. Flowchart of the Control System Code Implementation

3.7 Data Aquisition System

To evaluate the performance of the mechatronic control system in comparison to the mechanical system, a data acquisition system was developed. The purpose of the system was to collect relevant operational data from both control implementations in order to compare their performance. In particular, the data was intended to evaluate the ability of the proposed controller to address the stability and ride-height regulation issues identified in Section 1.2.

The primary focus of the data collection was IMU measurements, since these could be obtained in an equivalent manner for both the mechanical and mechatronic

systems. As mentioned in Section 2.7, ride height is defined in the Earth frame. Analysing the vertical acceleration in the Earth frame, $\ddot{z}_e$, could therefore provide information about oscillation and ride height stability.

This requirement also influenced the hardware design of the system. The encapsulated electronics box was therefore developed with a modular architecture, allowing it to be installed and removed independently of the mechatronic control hardware mounted on the boat.

3.7.1 Data Logging

The logging task was executed at 20 Hz, collecting and synchronizing data from three primary sources. From the IMU data, orientation vectors (quaternions) and linear acceleration were retrieved. The vertical acceleration in the Earth frame, $\ddot{z}_e$ seen in equation 2.15, computed on the MCU using the transformation logic described in Section 2.7.

Further, the GPS module provided UTC timestamps. By pairing these with the local MCU clock, samples could be tagged with an absolute time reference, allowing the logged samples to be correlated with external video recordings of the trials.

With the mechatronic system installed, the logging was extended to include measurements such as raw ADC wand values, filtered ride height estimates, and commanded servo angles. This enabled post flight analysis of the controller performance.

Logged data was written to a SD card via the SPI bus. To prevent data loss during potential power failures, an open-write close strategy was implemented. First samples were bufferd in RAM, once the buffer reached 20 samples or a two-second threshold was met, the data was flushed to a CSV file. Closing the file immediately between each write operation, ensured that an abrupt power disconnection would only result in the loss of the most recent two-second data buffer.

3.8 Field Trials

Two separate field trials were conducted to evaluate the system: one to establish a baseline of typical vessel dynamics and one to verify the functionality of the integrated mechatronic system.

3.8.1 Baseline Data Collection

Initial trials were conducted at the to characterize typical Moth dinghy dynamics. For this purpose, the hardware was mounted on a production Moth dinghy equipped with a conventional mechanical control system. During these tests, the system functioned exclusively as a data acquisition unit, recording hull dynamics via the onboard IMU. During these test, the weather conditions were favourable with steady wind sufficient to achieve foiling speeds.

3.8.2 System Verification

Subsequent trials were performed to evaluate the complete mechatronic system implemented on *Saga*. Due to insufficient wind speeds, the boat could not gain enough speed in order to start foiling. To address this issue, *Saga* was towed behind a powerboat. The powerboat provided enough speed for foiling to be initiated in short periods.

The focus of the field test was placed on hardware durability, data collection, and software implementation, rather than control system performance. Consequently, the proportional gain was intentionally increased to $k_p = 0.5$ prior to testing in order to produce exaggerated actuator movements across a larger portion of the available range. This made it easier to verify that the flap motions occurred in the correct direction and at the appropriate timing in response to changes of the wand signal.

4

Results

This chapter presents the findings from the field trials conducted with the mechatronic control system on the *Saga* Moth dinghy. The results are divided into three main areas to evaluate the project's objectives. First, the operational validation focuses on the system's physical integrity and the reliability of the data acquisition in a marine environment. Second, the foiling performance is analysed through high-frequency sensor data, evaluating the PID controller's behaviour and the closed-loop response during flight. Finally, a comparative analysis of vertical acceleration is presented, using data from a production Moth as a benchmark to contextualize the stability achieved by the developed system.

4.1 Operational Validation and Robustness

The mechatronic system successfully demonstrated its resilience in a harsh marine environment. The hardware housing, including the modified waterproof box and servo actuator, effectively protected the sensitive electronic components. The system survived full submerging in the water during the trial, confirming the effectiveness of the sealing strategies. Further the retrofitted components, such as the custom servo bracket and wand attachments, maintained structural integrity under the dynamic load.

Finally, the modular design of the data acquisition system was also successfully validated during testing. The control module could be installed on a different Moth dinghy with only minor modifications, demonstrating the portability of the system architecture. During the on-water trials, sensor and operational data were logged continuously without interruptions. This showed that both the data acquisition system and the waterproof enclosure worked reliably in practice.

4.2 Foiling Performance

During the flying state, the mechatronic system was observed actively adjusting the flap of the main foil in response to the surface measurements by the wand.

Figure 4.1 shows foiling sequences highlighted in green, as well as measured ride height, $\hat{z}$, servo motor command angle, α, and flap angle, δ. As the vessel approaches a height closer to the ride height target, the servo command gradually moves the flap towards a more neutral position reducing lift. This confirms that the PID controller effectively modulates the flap to maintain stability.

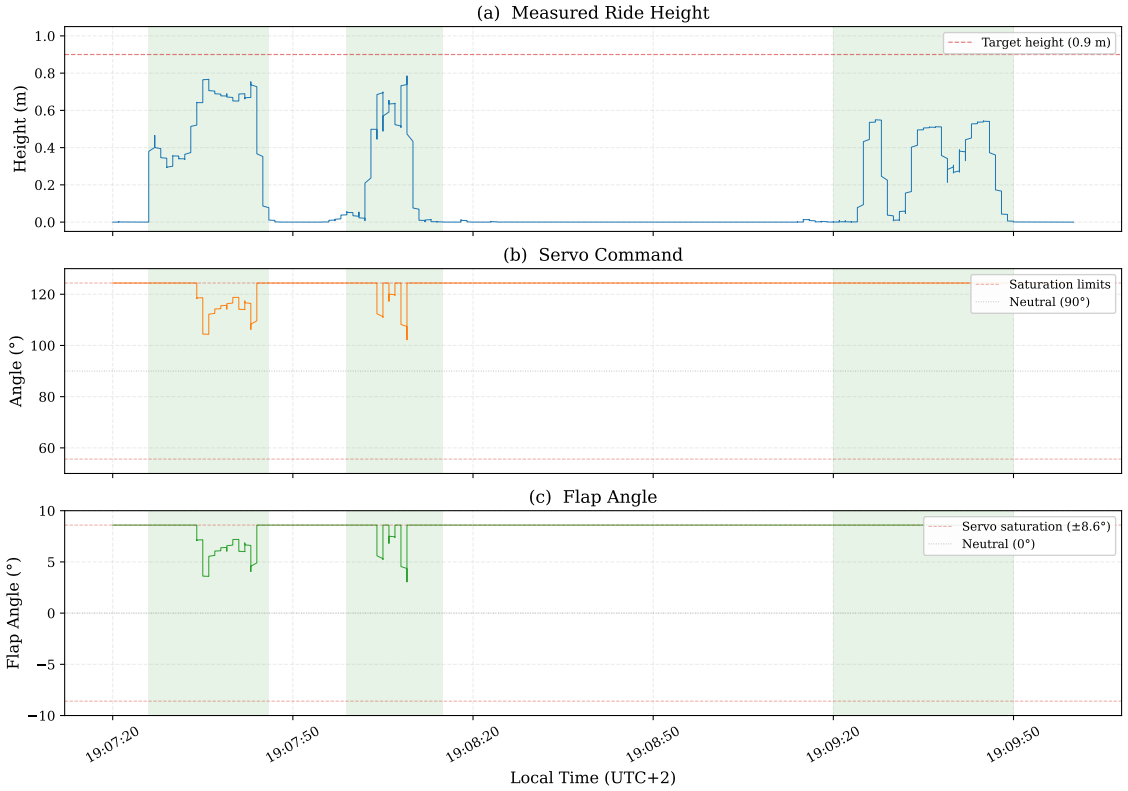

Figure 4.1. Foiling sequence

Figures 4.2 and 4.3 shows the foiling sequences zoomed in at 50ms between data points. The plots reveal several characteristics of the closed loop system during foiling flight.

The proportional band between ride height and flap angle, when not saturated demonstrated a strongly negative correlation, confirming the controller correctly reduces lift as height increases.

With a Kp = 0.5 and a target height of 0.9m, the PID output saturates at the ±8.64° limit whenever the height error exceeds approximately 0.28m, corresponding to a measured height of roughly 0.6m. In Period 1, the controller is saturated for 54% of the time, in Period 2, for 78% and 100% in Period 3. This is shown in 4.1. During saturation, the flap is held at its maximum angle of 8.64°, and the controller effectively operates in open loop. The flap only begins to modulate once the height exceeds approximately 0.6m, leaving a narrow operating window of 0.6-0.77m in which proportional control is active.

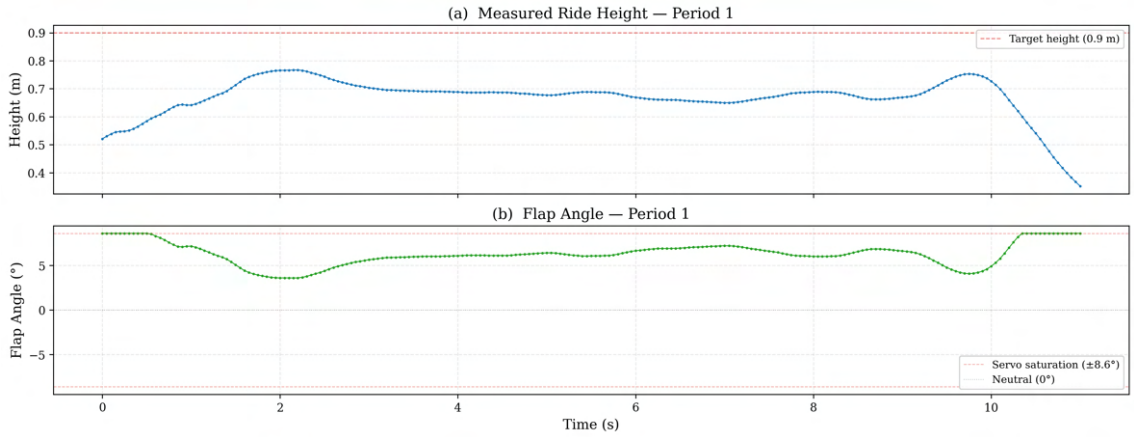

Figure 4.2. Period 1 active control in the Foiling sequence

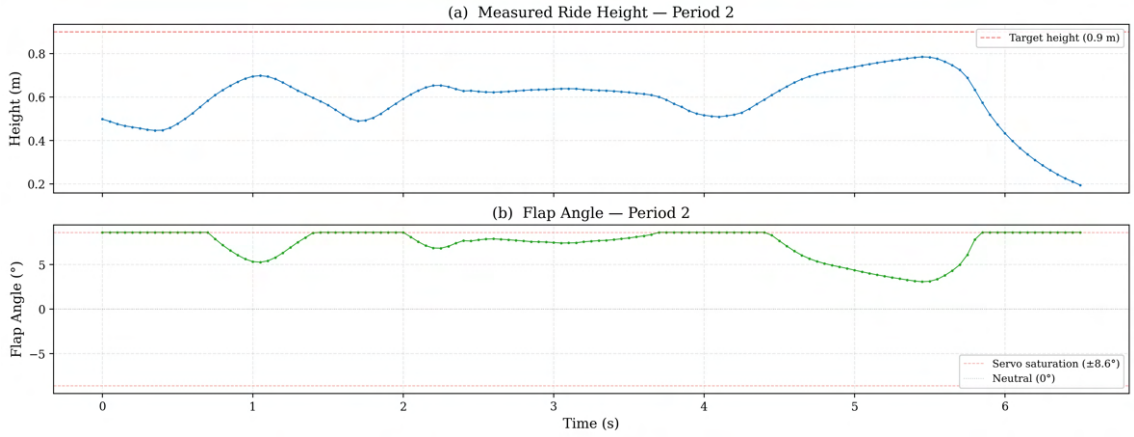

Figure 4.3. Period 2 active control in the Foiling sequence

Figure 4.4 shows the control error, e, (target height minus measured height) for both foiling periods, with the integral activation zone ($|e| < 0.1$ m) highlighted. The error signal remains above the 0.1 m threshold throughout both periods, with minimum values of 0.13 m and 0.12 m for Period 1 and Period 2, respectively.

As a result of this persistent deviation, the integral term is never allowed to accumulate; instead, it is continuously reset to zero by the anti-windup mechanism implemented in the PID controller. This operational constraint means the controller effectively functions as a PD controller during the entire trial duration.

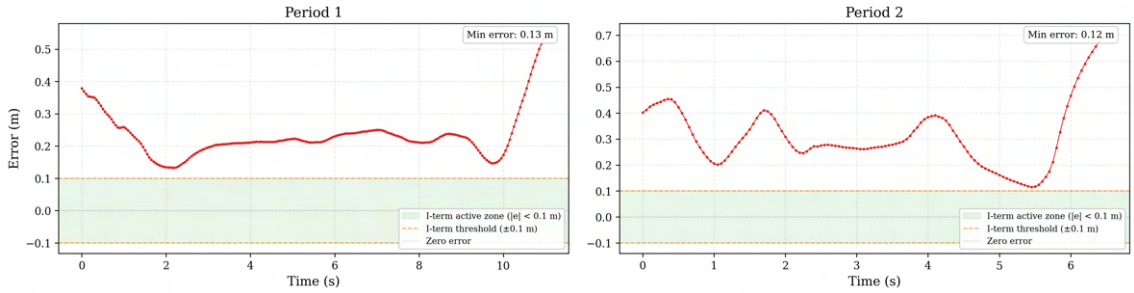

Figure 4.4. Error signal for Period 1 and 2

Figure 4.5 shows the relationship between ride height and flap angle during active control for both foiling periods. The lower panel shows the time derivatives of both signals, normalized to a common scale and with the flap derivative inverted to allow direct comparison.

The near complete overlap of the two derivatives demonstrates that height changes and flap corrections occur within the same logging interval. The cross correlation between the two yields $r = -0.9995$ at zero lag for Period 1 and $r = -0.9994$ for Period 2, with over 98% of samples exhibiting opposite sign derivatives in the same 50 ms sample.

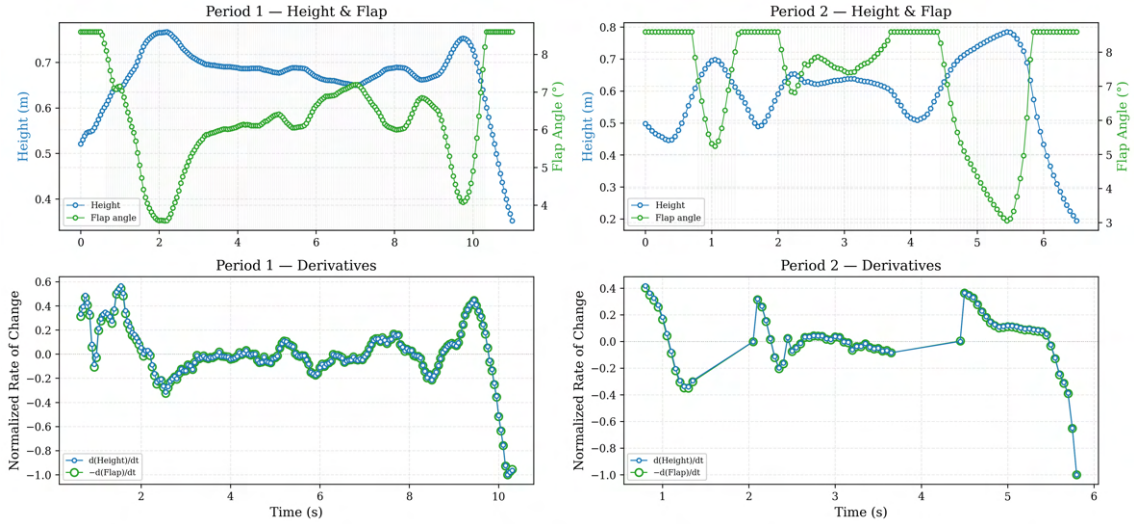

Figure 4.5. Control System Response

4.3 Vertical Acceleration Measurements

Figure 4.6 shows a comparison of vertical acceleration during foiling between *Saga* and a production Moth dinghy. Saga exhibited significantly lower vertical accelerations, with a standard deviation of 0.35 $\mathrm{m/s^2}$ in Period 1 and 0.26 $\mathrm{m/s^2}$ in Period 2, compared to 1.15 $\mathrm{m/s^2}$ for the production Moth.

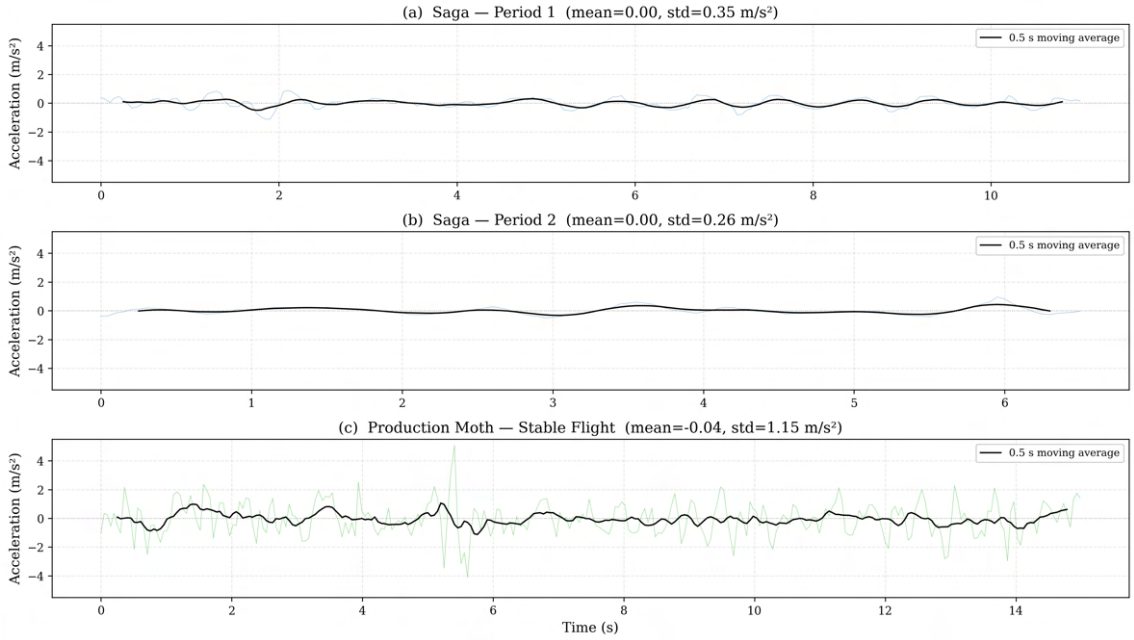

Figure 4.6. Vertical acceleration comparison between *Saga* and a production Moth during foiling

5

Discussion

This chapter discusses the results and methodology presented in the preceding chapters. Further it addresses limitations, concludes the thesis and finally suggests future work to advance the *Saga* platform.

5.1 Hardware Robustness and Computational Performance

The on-water trial demonstrated that the mechatronic system is mechanically durable and capable of surviving the marine environment, including full submersion. The core control loop from sensor to flap actuation functioned as designed.

The high correlation at zero lag suggests that the system introduces no significant phase delay relative to the boat's dynamics, as seen in Figure 4.5. Because the internal control loop executes at 100 Hz while the data logging is limited to 20 Hz, the total computational latency including ADC conversion, PID calculation, and PWM generation is confirmed to be below the 50 ms logging period. This frequency is high enough to capture and log the wand deflections reported in Section 3.5.2 according to Nyquist-Shannon sampling theory (see Section 2.4).

This validates the hardware accelerated approach using the BNO085 IMU and the LEDC hardware timers, as the offloading of sensor fusion and pulse generation effectively eliminated software induced timing jitter. Any further resolution of the system's latency would require a higher frequency logging implementation, but for the observed foiling speeds, the current latency is considered negligible.

5.2 Control Logic Evaluation

The flight durations of 6 and 11 seconds were insufficient for the system to reach a settled condition. No conclusion can therefore be drawn regarding the performance of the proposed control logic.

While the simulation results show the potential of the proposed control logic, it is not enough for verification of the real world system. The simulation was based on a linearised model, making the dynamics simplified and only valid around the operating point. Further, several coefficients implemented in the simulation were not experimentally validated, limiting the accuracy and physical representativeness of the model. Consequently, the tuning parameters, K_p, K_i, and K_d stemming from the simulation results, could not be validated for real life application.

5.3 Comparative Analysis with Production Moth

While the data presented in Figure 4.6 indicates a lower standard deviation in vertical acceleration for *Saga*, no definitive conclusions can be drawn regarding the superior performance of the mechatronic system from this comparison alone. The two datasets were recorded under significantly different and unquantified environmental conditions, including variations in wind velocity, wave state, and vessel speed.

Furthermore, a critical limitation in this analysis is that the production Moth data contains only IMU readings, with no corresponding flap angle or ride height measurements. This discrepancy makes it impossible to assess the closed loop response of the mechanical system or determine the exact ride height at which the vessel was operating.

As a result, the observed stability on *Saga* cannot be isolated as a product of the control logic, as it may depend on lower foiling speed and calmer sea state during trial. A meaningful performance benchmark would require a synchronized logging architecture of both vessels and operation under identical conditions, to accurately determine the efficiency of the mechatronic control system over the purely mechanical setup. Therefore, no conclusions can be drawn on the performance of a mechatronic control system compared to a mechanical one.

5.4 Systemic and Methodological Limitations

The data in Figure 4.1 showed the wand measurement in foiling sequence (Period 1), abruptly transition from 0 to approximately 0.4 m when the boat lifts off, rather than increasing gradually. This is likely caused by a misalignment between the magnet and the encoder reader in the sensor housing. However this cause is not certain and requires further testing to be proven.

It should be noted that the logged data records the servo command rather than the actual flap position. The reported time between change in height and flap angle reflects the computational pipeline only. The servo actuator introduces additional mechanical delay as it moves the flap against hydrodynamic forces. Characterising the actuator delay would require direct measurement of the servo position, which was not available in the current setup.

A notable constraint in the current analysis of the control system was that the GPS

module was primarily utilized for establishing a Universal Time Coordinated (UTC) anchor. While this allowed for synchronization between the high-frequency control logs and external video recordings, Speed Over Ground (SOG) was not included in the data acquisition pipeline.

The lift force produced by the foil is quadratically dependent on velocity (v^2), as defined in Equation 2.2. Because velocity was not logged, it is difficult to isolate the primary driver of the vessel's vertical dynamics during the trials. Without a synchronized velocity correlate, it is not possible to determine whether a change in vertical acceleration ($\ddot{z}$) was a direct result of a flap adjustment (δ) or a subtle fluctuation in boat speed.

5.5 Conclusion

The primary objective of this thesis was to design and implement a mechatronic ride height control and data acquisition system for the Moth dinghy *Saga*. By integrating embedded systems with custom hardware, the project successfully transitioned the vessel from a purely mechanical platform to a programmable mechatronic system.

The project's particular objectives were addressed as follows:

- **Data Acquisition:** A platform for measuring and collecting high resolution data on ride height and vessel dynamics was fully realized, transforming the previous mechanical setup into a transparent, data driven system.
- **Mechatronic System:** The implementation of a mechatronic system capable of active flap modulation was validated. The system demonstrated mechanical resilience and operational integrity in a marine environment.
- **Height Control:** A PID-based control loop was successfully implemented with minimal latency. However, due to insufficient foiling time during trials, the system didn't reach a settled condition. Consequently, the system's ability to maintain steady ride height remains unverified.
- **Performance Benchmarking:** A definitive comparison against the mechanical system could not be established. While the mechatronic platform offers more adjustability, the lack of identical testing conditions meant its theoretical performance advantages remain a subject for future validation.

In summary, this thesis has established a mechatronic foundation for *Saga*. Although final performance benchmarking is pending, the transition to a programmable control architecture represents a technological leap for CFSail's future development.

5.6 Future Work

An area for future work is continued experimental validation and controller tuning through controlled on-water testing. Due to the limited availability of suitable

weather conditions, personnel and testing opportunities, the field testing conducted during the project was insufficient for fully validating the controller performance. Additional testing would allow the regulator parameters to be refined iteratively until satisfactory foiling behaviour and stability are achieved under real operating conditions.

Further experimental testing would also enable the development of a more realistic and experimentally validated vessel model. The current simulation model relies heavily on theoretical assumptions and estimated parameters, limiting both its accuracy and predictive capability. Through system identification and experimental measurements, more representative hydrodynamic parameters could be obtained and incorporated into the simulation environment. This would improve the realism of the model and enable more reliable controller tuning in simulation before conducting time consuming field tests.

A critical technical improvement for future iterations is the integration and high frequency logging of boat velocity, such as Speed Over Ground (SOG). As discussed, the lift force is quadratically dependent on velocity (v^2), and without synchronized velocity data, it remains difficult to isolate the effects of flap adjustments from fluctuations in speed. By logging real time velocity alongside control signals, future research could generate empirical lift coefficient curves and quantify flap authority with much higher precision.

With a more accurate vessel model and velocity data, more advanced control strategies could also be investigated. Methods such as model based control, state-space control and adaptive control may improve system performance under varying operating conditions and wave disturbances. Such approaches would likely require improved state estimation and more physically accurate measurements of the vessel motion.

Future work could therefore include the integration of additional sensors to create a more complete control system for the vessel. Combining measurements from multiple sensors may improve robustness, state estimation and disturbance rejection through more advanced sensor fusion techniques.

Bibliography

[1] BK Yacht Design, *A Deep Dive into Hydrofoils and Planing Hulls*, Oct. 2023. [Online]. Available: https://bkyachtdesign.com/a-deep-dive-into-hydrofoils-and-planing-hulls/.

[2] S. Tavakoli, M. Zhang, A. A. Kondratenko, and S. Hirdaris, "A review on the hydrodynamics of planing hulls," *Ocean Engineering*, vol. 303, p. 117 046, Jul. 2024, ISSN: 0029-8018. DOI: 10.1016/J.OCEANENG.2024.117046.

[3] J. R. Meyer, *Hydrofoil overview-a brief tutorial*, New York, Jan. 2018. [Online]. Available: https://www.foils.org/wp-content/uploads/2018/01/HY-Tutorial.pdf.

[4] B. Horel, "System-based modelling of a foiling catamaran," *Ocean Engineering*, vol. 171, pp. 108–119, Jan. 2019. DOI: 10.1016/j.oceaneng.2018.10.046.

[5] C. H. Lewis, *Hydrofoils and Hydrofoil Craft*, 1st ed. Berlin: Springer-Verlag, 1988.

[6] B. Li et al., "Study of the double closed-loop active disturbance rejection control strategy for the longitudinal motion of fully submerged hydrofoil craft," *Ocean Engineering*, vol. 315, p. 119 714, Jan. 2025. DOI: 10.1016/J.OCEANENG.2024.119714.

[7] R. Walker, *The History of Hydrofoils*, May 2023. [Online]. Available: https://www.mewburn.com/forward/the-history-of-hydrofoils.

[8] *Hydrofoil*, May 2026. [Online]. Available: https://en.wikipedia.org/wiki/Hydrofoil.

[9] *The America's Cup*. [Online]. Available: https://www.americascup.com/the-americas-cup.

[10] Candela Technology AB, *Foiling System and Flight Controller Technology*. [Online]. Available: https://candela.com/technology/.

[11] *Sailing hydrofoil*, Dec. 2025. [Online]. Available: https://en.wikipedia.org/wiki/Sailing_hydrofoil.

[12] D. Anderson and S. Eberhardt, "How airplanes fly: A physical description of lift," *Sport Aviation*, vol. 1, 1999. [Online]. Available: https://cadmac.co.uk/index_htm_files/how_airplanes_fly.pdf.

[13] J. M. K. Godø, S. Steen, and O. M. Faltinsen, "A resistance model for hydrofoil fast ferries with fully submerged foil systems," *Ocean Engineering*, vol. 301, p. 117 503, Jun. 2024, ISSN: 0029-8018. DOI: 10.1016/J.OCEANENG.2024.117503.

[14] Aygor Teksen, "Analyses of Foil Configurations of IMOCA Open 60s with Towing Tank Test Results," Ph.D. dissertation, University of Liège, Liege, 2017. [Online]. Available: http://hdl.handle.net/2268.2/4411.

[15] I. Campbell, M. Owen, and G. Provinciali, "Dagger-board evaluation for an IMOCA 60 yacht," *Ocean Engineering*, vol. 90, pp. 2–10, Nov. 2014, ISSN: 0029-8018. DOI: 10.1016/J.OCEANENG.2014.06.042.

[16] *Classes & Designs*, Mar. 2026. [Online]. Available: https://www.sailingclubmanager.com/boats-classes-fleets/classes-designs.

[17] "International Moth Class Rules," International Sailing Federation (ISAF), London, GBR, Tech. Rep., Dec. 2024.

[18] International Moth Class Association, *GENERAL MOTH CLASS INFORMATION*. [Online]. Available: https://www.moth-sailing.org/blank-7.

[19] SuMoth Challenge Team, *SuMoth Challenge*, 2026.

[20] Foiling SuMoth Association, *2023 Foiling SuMoth Challenge: Rules v23r1.1*, Av. de Severy 13, 1004 Lausanne, Switzerland, 2023. [Online]. Available: https://www.scribd.com/document/771193090/Foiling-SuMoth-Rules-v23r1-1.

[21] Liru Zan, Hanbing Sun, Shijie Lu, Jin Zou, and Lei Wan, "Experimental Study on Porpoising of a High-Speed Planing Trimaran," *Journal of Marine Science and Engineering*, vol. 11, pp. 7–69, Mar. 2023. DOI: 10.3390/jmse11040769.

[22] D. McLean, "Aircraft flight control systems," *The Aeronautical Journal*, vol. 103, pp. 159–166, Mar. 1999. DOI: https://doi.org/10.1017/S0001924000064976.

[23] Eun Jung Chae and Yin Lu Young, "Influence of spanwise flexibility on airfoils and hydrofoils," *Physics of Fluids*, vol. 33, pp. 67–124, Jun. 2021. DOI: 10.1063/5.0052192.

[24] W. S. Aboud, S. M. Haris, and Y. Yaacob, "Advances in the control of mechatronic suspension systems," *Journal of Zhejiang University-SCIENCE C*, vol. 15, no. 10, pp. 848–860, Jan. 2014. DOI: 10.1631/jzus.C14a0027.

[25] R. Bencatel, S. Keerthivarman, I. Kolmanovsky, and A. R. Girard, "Full State Feedback Foiling Control for America's Cup Catamarans," *IEEE Transactions on Control Systems Technology*, vol. 29, no. 1, pp. 1–17, Mar. 2021. DOI: 10.1109/TCST.2019.2955059.

[26] J. Bai and Y. Kim, "Control of the vertical motion of a hydrofoil vessel," *Ships and Offshore Structures*, vol. 5, no. 3, pp. 189–198, Sep. 2010, ISSN: 17445302. DOI: 10.1080/17445300903354224.

[27] I. Chatzakis, "Motion Control of High-Speed Hydrofoil Vessels Using State-Space Methods," Ph.D. dissertation, Massachusetts Institute of Technology, Cambridge, MA, 2004. [Online]. Available: http://hdl.handle.net/1721.1/33429.

[28] S. H. Kim and H. Yamato, "An experimental study of the longitudinal motion control of a fully submerged hydrofoil model in following seas," *Ocean Engineering*, vol. 31, no. 5-6, pp. 523–537, Apr. 2004, ISSN: 00298018. DOI: 10.1016/j.oceaneng.2003.10.003.

[29] C. Miller, "Moth Electronic Wand System: Control System for International Moth on Hydrofoils," BoatDesign.net / Glasgow University report, Tech. Rep., 2025. [Online]. Available: https://www.boatdesign.net/attachments/moth-electronic-wand-system-pdf.89499/.

[30] J. Lan, J. Cho, D. Erdogmus, J. C. Principe, M. A. Motter, and J. Xu, "LOCAL LINEAR PID CONTROLLERS FOR NONLINEAR CONTROL," *Control and intelligent systems*, vol. 33, pp. 26–35, Jan. 2005. DOI: 10.2316/Journal.201.2005.1.201-1541.

[31] T. Glad, L. Ljung, and V.-D. (.-b. collection), *Control theory [electronic resource] : multivariable and nonlinear methods / Torkel Glad and Lennart Ljung.* eng. Taylor & Francis, Jan. 2000, ISBN: 0203484754. [Online]. Available: https://research.ebsco.com/linkprocessor/plink?id=888840a1-f158-3364-b189-7c24967a1c79.

[32] T. H. Karl Johan Åström, *Advanced PID Control*, 1st ed. USA: ISA (Instrumentation, Systems, and Automation Society), 2006, ISBN: 978-1556179426.

[33] R. W. S. Alan V. Oppenheim, *Discrete-Time Signal Processing*, 3rd. Pearson, 2010, ISBN: 978-0131988422.

[34] A. Thålin, "Extended Kalman Filter as Observer for a Hydrofoiling Watercraft Modelling of a new hydrofoiling concept, based on the Spherical Inverted Pendulum Model," Ph.D. dissertation, KTH Royal Institute of Technology, Stockholm, 2022. [Online]. Available: https://kth.diva-portal.org/smash/record.jsf?pid=diva2%3A1728676&dswid=-2612.

[35] D. Simon, *Optimal State Estimation: Kalman, H-infinity, and Nonlinear Approaches*. Hoboken, N.J.: Wiley-Interscience, 2006, ISBN: 978-0471714651.

[36] *1057-2017 - IEEE Standard for Digitizing Waveform Recorders*, Jan. 2018. DOI: 10.1109/IEEESTD.2018.8291741.

[37] G. James, *Advanced modern engineering mathematics*, 4th ed. USA: Prentice Hall, 2011, pp. 676–699, ISBN: 9780273719236.

[38] D. Rapos, C. Mechefske, and M. Timusk, "Dynamic sensor calibration: A comparative study of a Hall effect sensor and an incremental encoder for measuring shaft rotational position," in *2016 IEEE International Conference on Prognostics and Health Management (ICPHM)*, 2016, pp. 1–5. DOI: 10.1109/ICPHM.2016.7542858.

[39] Z. Yu, A. Mohammed, and I. Panahi, "A Review of Three PWM Techniques," in *American Control Conference*, Albuquerque, NM, USA: IEEE, 1997, pp. 257–261. DOI: 10.1109/ACC.1997.611797.

[40] H. Jiang, M. Zhu, Y. Fu, and Y. Wu, "iNavFIter-M: Matrix Formulation of Functional Iteration for Inertial Navigation Computation," *IEEE Transactions on Aerospace and Electronic Systems, Aerospace and Electronic Systems, IEEE Transactions on, IEEE Trans. Aerosp. Electron. Syst.*, vol. 61, pp. 18 756–18 771, Dec. 2025, ISSN: 0018-9251. DOI: 10.1109/TAES.2025.3615189.

[41] Giorgio C. Buttazzo, *Hard Real-Time Computing Systems: Predictable Scheduling Algorithms and Applications*. Springer Science & Business Media, 2011. DOI: 10.1007/978-1-4614-0676-1.

[42] J. Valvano, *Embedded Systems: Introduction to Arm Cortex-M Microcontrollers*, 1st. CreateSpace Independent Publishing Platform, 2012, ISBN: 978-1477508992.

[43] J. Graham-Jones and J. Summerscales, *Marine applications of advanced fibre-reinforced composites*, 1st ed. Cambridge: Woodhead publishing, 2016, ISBN: 9781782422501. DOI: 10.1016/C2013-0-16504-X.

[44] O. H. Margoto and A. S. Milani, "Comparing flax fibre/biopolymer woven composites with carbon fibre-enhanced, partially green alternatives: Mechanical performance versus sustainability," *Composites Part C: Open Access*, vol. 16, pp. 100–547, Mar. 2025. DOI: 10.1016/j.jcomc.2024.100547.

[45] F. C. Campbell, *Manufacturing processes for advanced composites*. Elsevier, 2004. DOI: https://doi.org/10.1016/B978-1-85617-415-2.X5000-X.

[46] Chalmers Formula Sailing, "Report of foil parameters from simulations(internal report)," English, Göteborg, Tech. Rep., 2026.

A

Models

A.1 Complete Simulink Model

The subsections *Wand*, and *Waves* are presented in figure A.1

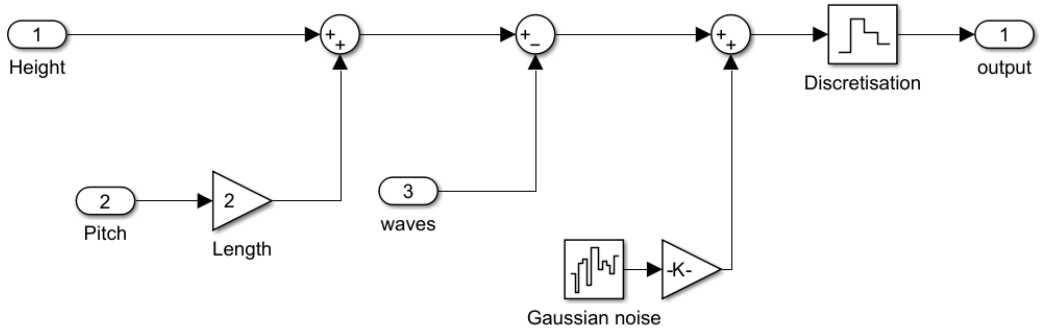

(a) The 'Wand' subsystem implemented in simulink

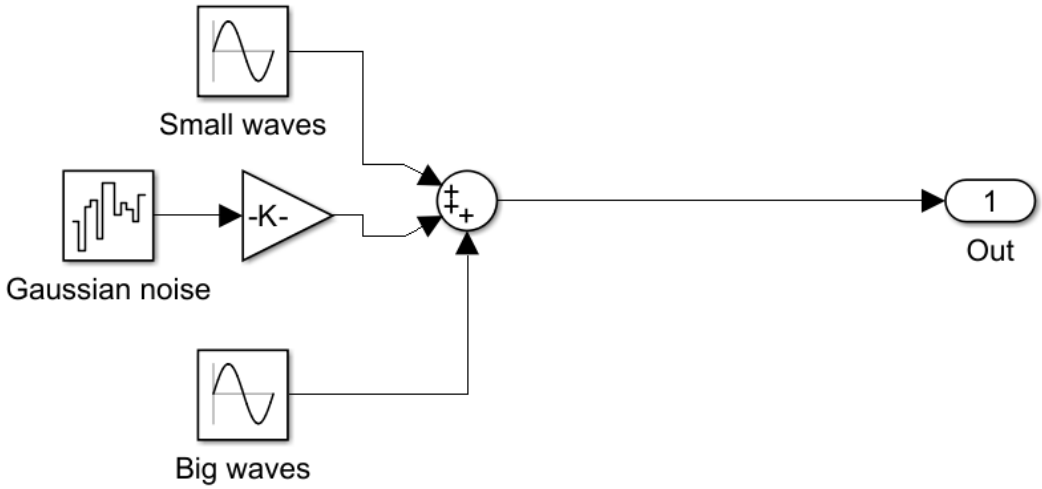

(b) The 'Waves' Subsection implemented in simulink

Figure A.1. Implementation of subsystems in simulink

B

Drawings and Schematics

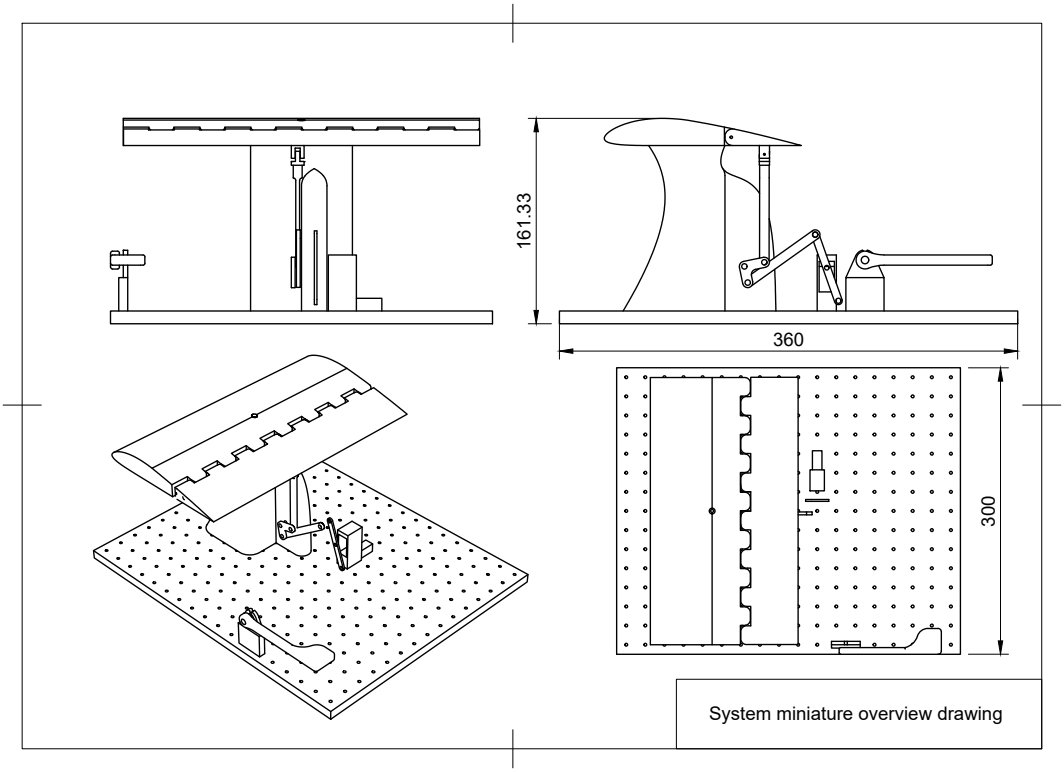

Figure B.1. CAD drawing of the miniature mechatronic system constructed early in the project

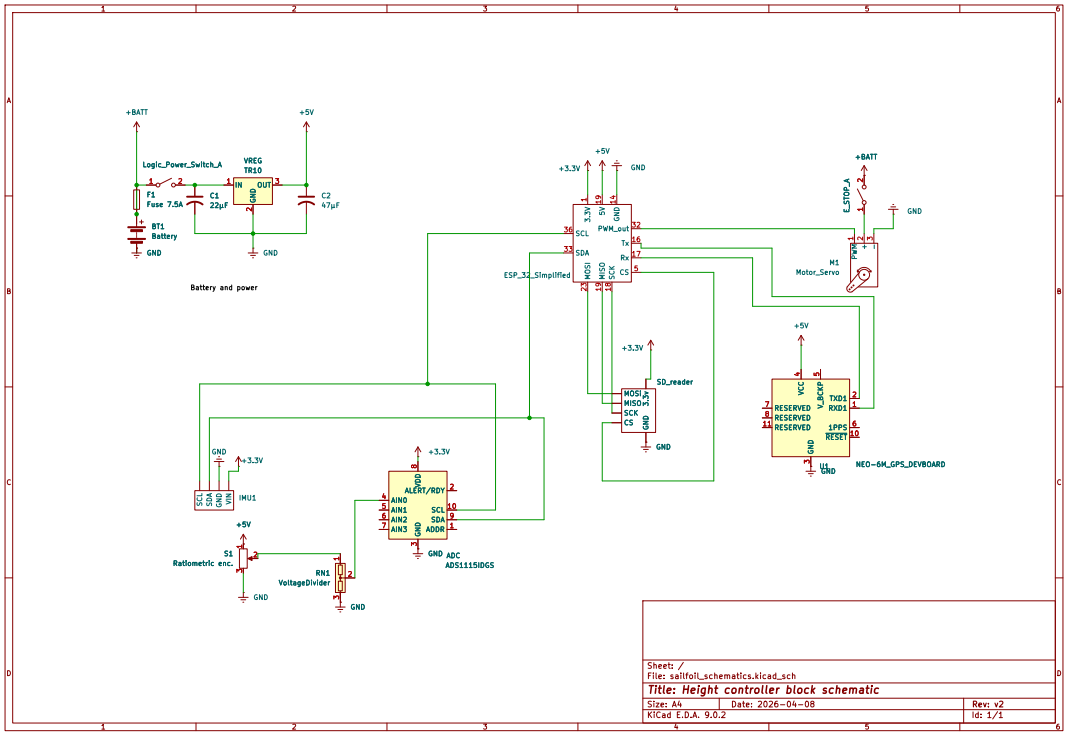

Figure B.2. Electrical schematic of control system

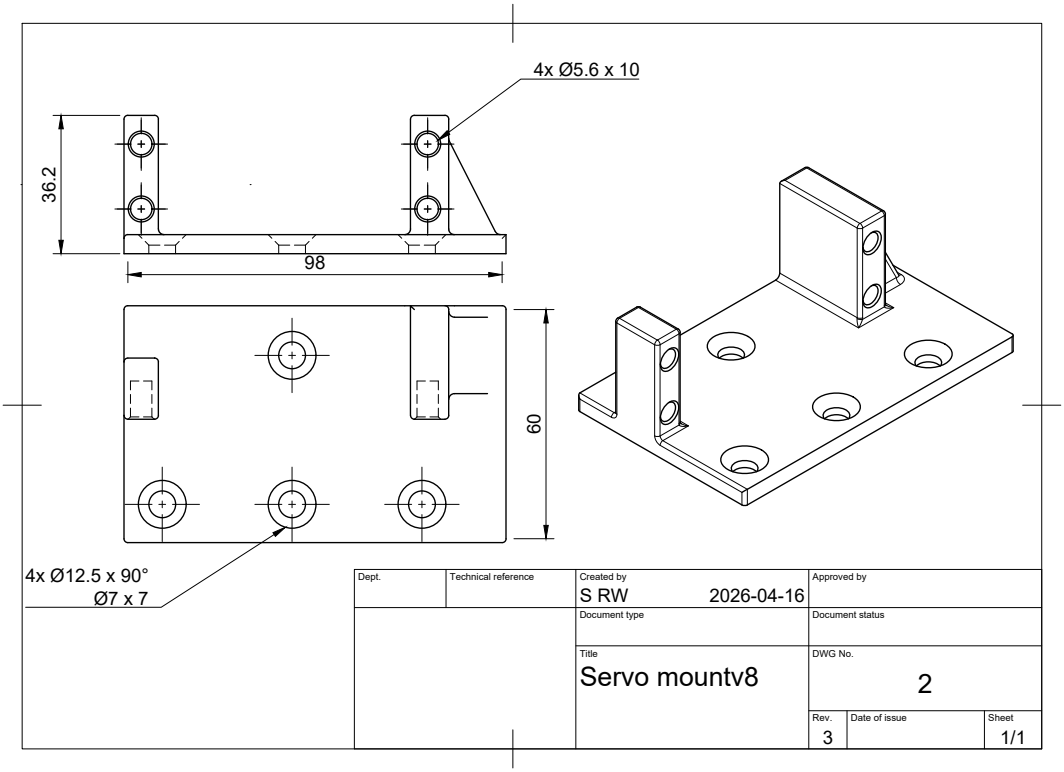

Figure B.3. Drawing detailing the Servo mounting bracket

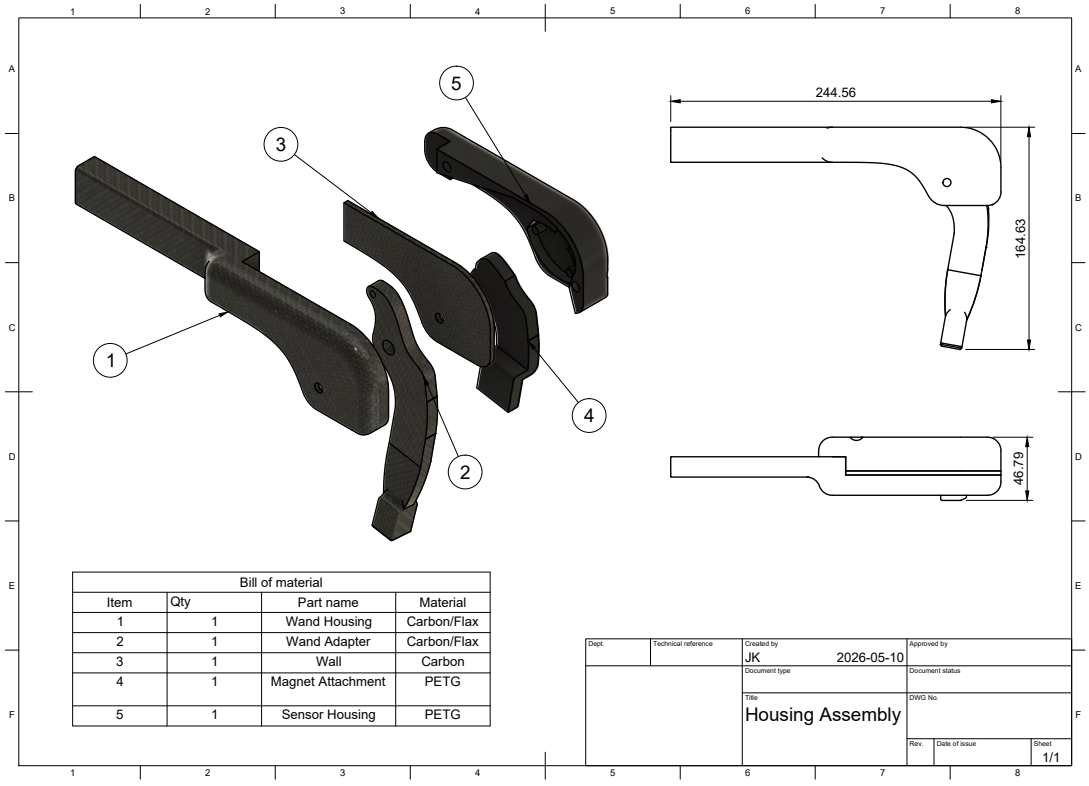

Figure B.4. Assembly drawing of wand and sensor housing

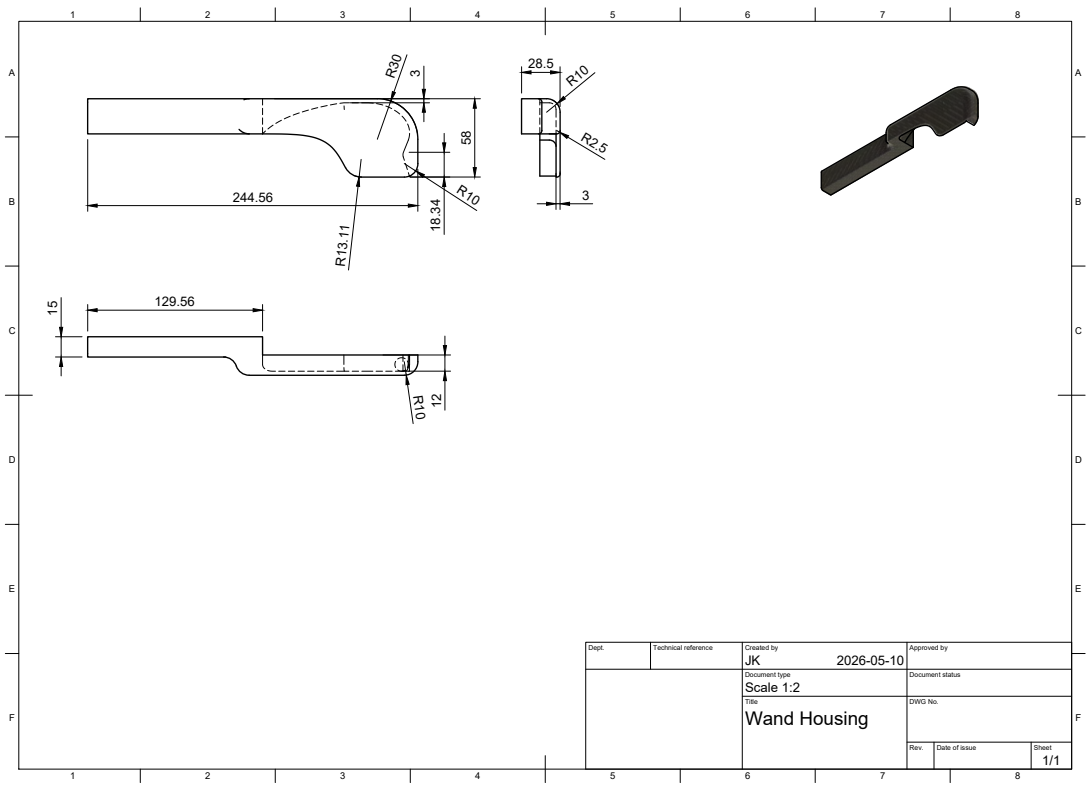

Figure B.5. Drawing of wand housing

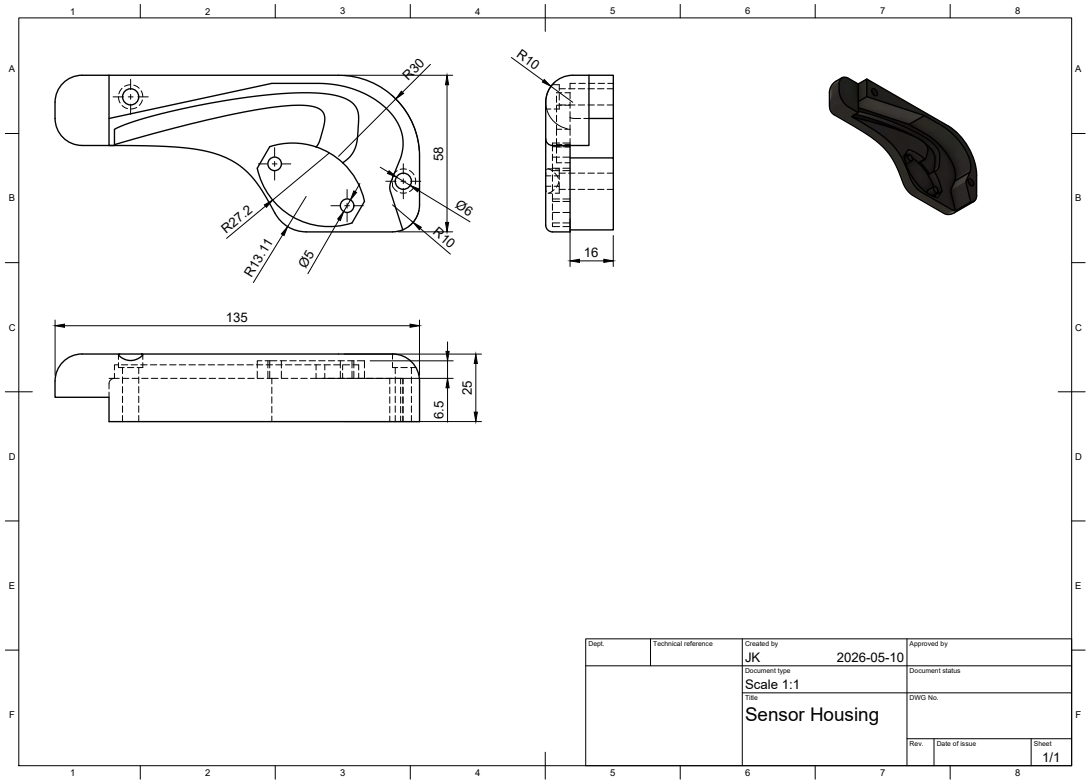

Figure B.6. Drawing of sensor housing

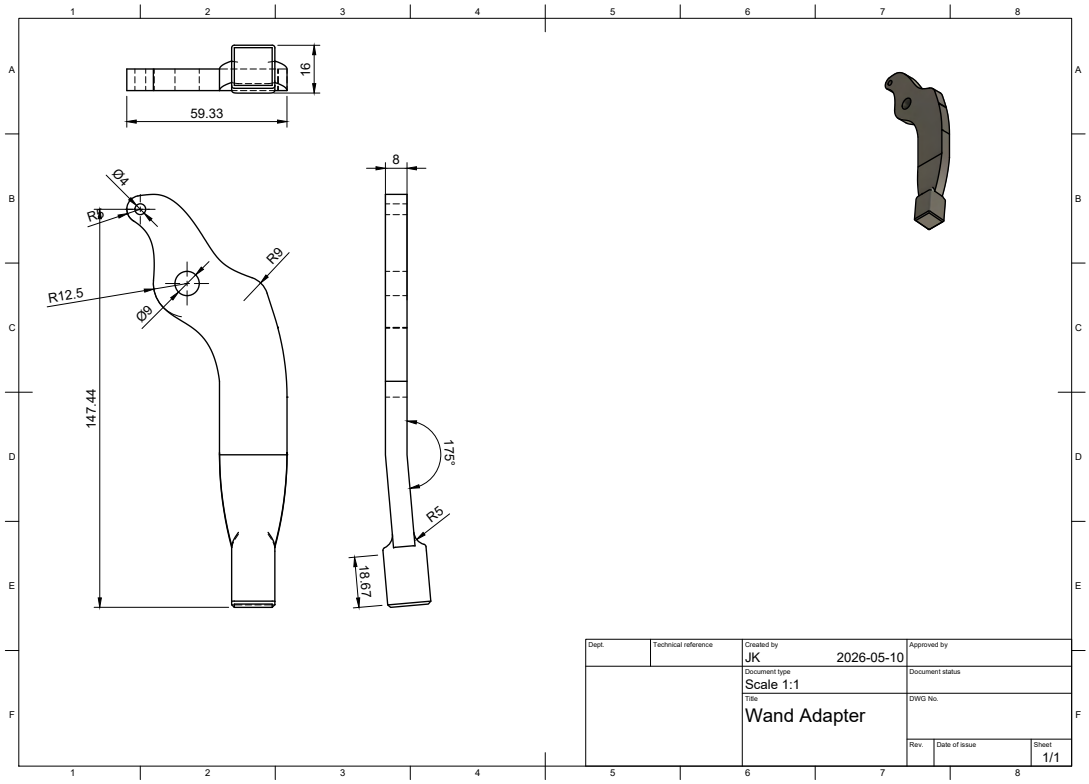

Figure B.7. Drawing of wand adapter

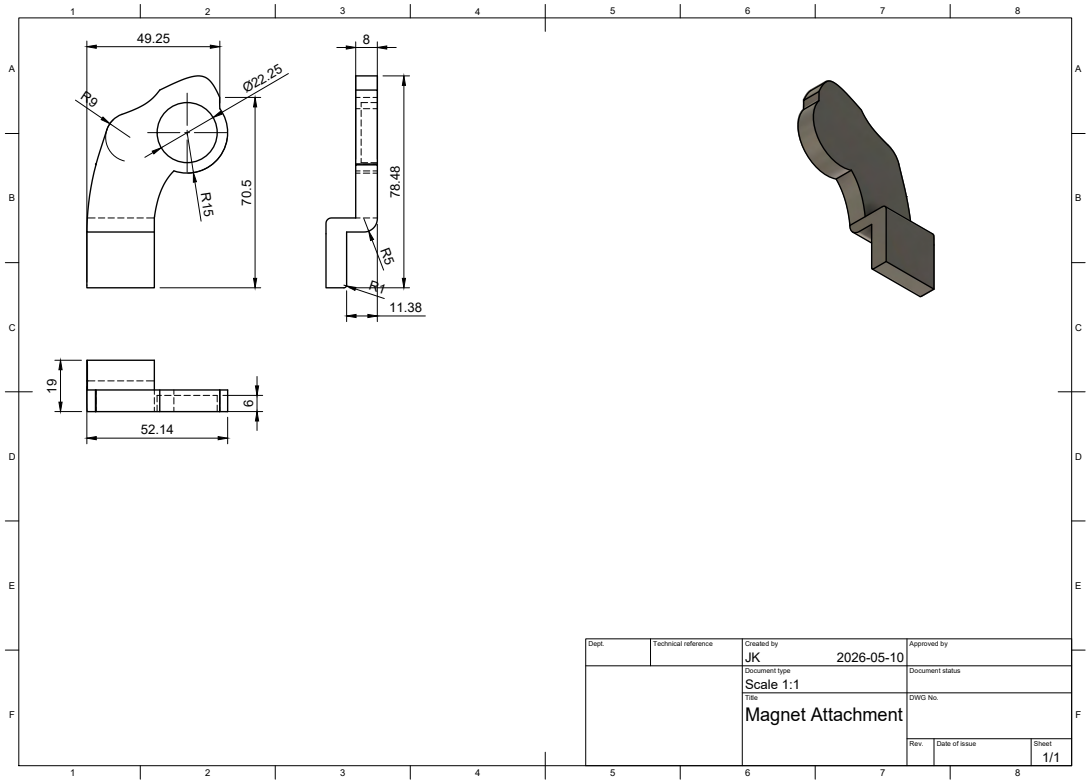

Figure B.8. Drawing of magnet attachment

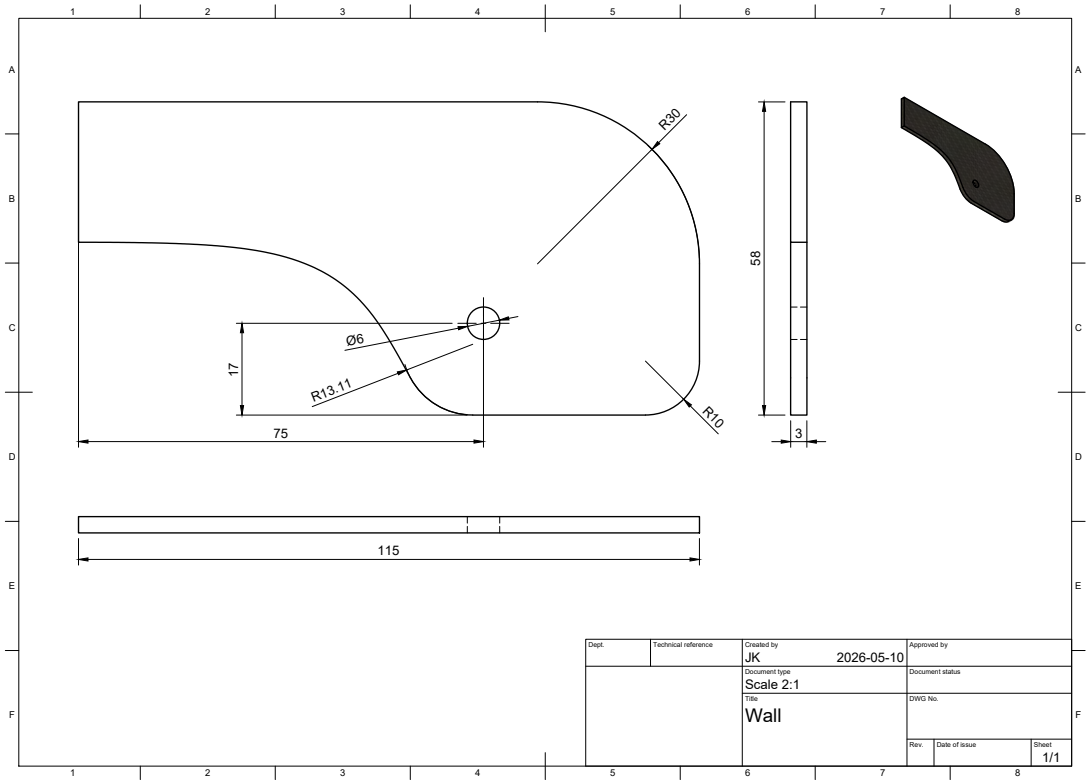

Figure B.9. Drawing of housing wall